

University of Nevada, Reno

Trolling Mode Technique
Long Tip Dynamics for the Contact Resonance Theoretical Model

A thesis submitted in partial fulfillment of the
requirements for the degree of Master of Science in
Mechanical Engineering.

by

Tony J. Moreno

Dr. Ryan Tung Thesis Advisor

August, 2019



THE GRADUATE SCHOOL

We recommend that the thesis
prepared under our supervision by

Entitled

be accepted in partial fulfillment of the
requirements for the degree of

, Advisor

, Committee Member

, Graduate School Representative

David W. Zeh, Ph.D., Dean, Graduate School

Abstract

The field of Atomic Force Microscopy (AFM) continues to grow in application and development due to the vast amount of research performed over the past three decades. The measurement capabilities and measurement methodologies of AFM continue to expand and far surpass the original capabilities of its 1986 inception. An in-depth exploration of the capabilities of AFM has resulted in the development of innovative data acquisition methods accompanied by the use of theoretical models in order to accurately interpret results. One of these methods is Contact Resonance Atomic Force Microscopy (CR AFM) and is characterized by its ability to retrieve mechanical properties of materials such as Young's Modulus of Elasticity. CR AFM utilizes a mathematical model designed using the physical and geometrical parameters of the AFM probe. Although the compilation of this novel microscopy research has proven to rapidly increase the versatility AFM, the main challenges that characterize the field of nanotechnology are still present. Since working with samples whose dimensions are in the nanoscale presents a challenge for sample interaction and examination, new AFM techniques, such as the Trolling Mode Technique (TMT) have been developed. The use of TMT involves physically modifying the traditional AFM probe to overcome some of the inherent challenges nanotechnology poses. In this document, we present an updated theoretical model for the CR AFM method, specifically tailored for the use of the TMT experimental setup during a CR AFM viscoelastic property retrieval trial. We derive the mathematical model and provide calibration for the parameters required in order to utilize the model. We then, verify the accuracy of our model by comparing our results to a 3D finite element model. Through this investigation, we create an updated CR AFM model which can be implemented for TMT that provides a higher degree of accuracy than the traditional model.

Acknowledgments

First and foremost I would like to acknowledge my parents Ing. Jesus Jaquez Perez and Ing. Sonia Moreno Cabral. From a young age my parents instilled in me a deep respect and appreciation for education. Their unconditional support and guidance has been key in this journey I embarked on 8 years ago. I will always be extremely thankful and humbled by the opportunities presented to me that have led to me where I'm at. So one big thank you to my parents for helping me cultivate values and resilience. My most deep gratitude and admiration to them.

Second I would like to thank my wife, Mariya Zagainova. The light that you have brought to my life truly shines as bright as the sun. This journey would have not been the same without you. There is not a single day that goes by where I don't look at you and rejoice for what we have. Infinite gratitude for your endless love and nurturing.

Third my adviser and mentor Dr. Tung who still up to date is probably the coolest professor I've had the pleasure to have class with. Extremely dedicated to his craft, and unarguably a very kind person. As an adviser and mentor, I have to thank him for being extremely patient with me, for I am one to get frustrated and flustered easily. The learning curve as a graduate student was definitely steep, but you helped me every inch of the way and for that I am extremely grateful. Will most definitely miss our impromptu meetings and interesting chats.

Last but not least I have a following list of professors, followed by a list of people, after 8 years at this university I've developed so many amazing relationships with people that I will forever take with me.

Dr. Wang, Dr. Vollstedt, Dr. Padilla, Dr. Aureli, Dr. Logan, Kelly Doyle, Leslie, Lana and the legendary Tom Gordon.

TABLE OF CONTENTS

	Page
Abstract	i
Acknowledgments	ii
LIST OF TABLES	v
LIST OF FIGURES	vi
1 Introduction	1
1.1 Background	1
1.2 Introduction to Non-optical Microscopy: Atomic Force Microscopy and The Scanning Tunneling Microscope	2
1.3 Force Response and Modes of AFM	6
1.4 Trolling Mode	12
1.5 Contact Resonance Atomic Force Microscopy: The Theoretical Model	14
2 Trolling Mode: A Contact Resonance Approach	17
2.1 3D Finite Element Model	17
2.2 Euler-Bernoulli Beam Model	20
2.3 Calibration: Non-dimensional Parameters \hat{I}, Δ and α	31
2.3.1 Non-dimensional Parameter \hat{I} : Torsional Trolling	32
2.3.2 Non-dimensional Parameter Δ : Free Vibrations	41
2.3.3 Non-dimensional Parameter $\beta_n L$: Frequency Ratios to Predict α	45
2.4 Updating the Theoretical Model for Non-circular Cross Sections	50
2.4.1 Updating \hat{I}_t and \hat{I} for Non-circular Cross Sections	50
2.4.2 Updating Δ for Non-circular Cross Section	53
2.4.3 Updating βL and New Predictions of α	53
3 Results	56

	Page
3.1 Baseline Model: Predictions for α	56
3.1.1 Using the First Mode of Transverse Vibration	56
3.1.2 Using the Second Mode of Transverse Vibration	59
3.2 Proposed Model: Predictions for α	61
3.2.1 Using the First Mode of Transverse Vibration	61
3.2.2 Using the Second Mode of Transverse Vibration	63
3.3 Updated Non-circular Cross Sectional Area Model: α Predictions	65
3.3.1 Using the First Mode of Transverse Vibration	65
3.3.2 Using the Second Mode of Transverse Vibration	67
3.4 Discussion: Percent Error for Effective Range of α	70
3.4.1 First Mode Discussion	70
3.4.2 Second Mode Discussion	71
4 Future Work	74
Conclusion	76
REFERENCES	78

LIST OF TABLES

Table	Page
2.1 Summary of results for calculated free eigenvalues through means of the no-spring, free version of our proposed model and results for the contact and free frequencies retrieved from the 3D finite element model.	48
2.2 Summary of results for calibration procedure.	48
2.3 Summary of results for first mode prediction procedure.	49
2.4 Summary of results for calculated free eigenvalues through means of the no-spring, free updated version of our proposed model for non-circular cross sectional areas and results for the contact and free frequencies retrieved from the 3D finite element model.	54
2.5 Summary of results for updating procedure for non-circular cross sectional areas.	55
2.6 Summary of results for first mode non-circular cross sectional areas prediction procedure.	55

LIST OF FIGURES

Figure	Page
1.1 STM Constant Height Mode, showing constant path of tip [dotted line] and varying current values [solid line].	3
1.2 STM Constant Current Mode, showing the path of the tip following the contour of the sample surface with constant tunneling current.	4
1.3 Mounted microcantilevered beam in net-repulsive contact with the sample.	7
1.4 Mounted microcantilevered beam in attractive regime with the sample due to van der Waals forces.	8
1.5 Force Curve Response for the microcantilevered beam compared to the van der Waals and Coulomb interactions	10
1.6 Trolling Mode Technique experimental setup with piezo stack element, photodiode, needle tip and submerged sample.	13
1.7 Euler-Bernoulli Beam Baseline Theoretical Model for CR AFM Young's modulus retrieval technique, where $w(x, t)$ represents the transverse displacement over time of the model and k is the stiffness coefficient for the spring.	15
2.1 3D Finite Computer Model for TMT Experimental Setup in the third mode of transverse vibration.	18
2.2 3D Finite Computer Model for TMT Experimental Setup in the third mode of transverse vibration.	19
2.3 Proposed Theoretical Model for Implementation of TMT for CR AFM where $w(x, t)$ represents the transverse displacement over time of the model, k is the stiffness coefficient for the spring, m is the added mass of the nanoneedle and I_o is the mass moment of inertia of the nanoneedle.	20
2.4 Flow chart depicting procedure for predictions of α . By inputting a free and a contact natural frequency along with the corresponding non-dimensional solution ($\beta_n L$) into the theoretical mode, we can make predictions once our non-dimensional parameters \hat{I} and Δ are calibrated. . . .	31

Figure	Page
2.5 Proposed Theoretical Model for Implementation of TMT for CR AFM, where $\theta(x, t)$ is the torsional displacement for the model and I_o is the mass moment of inertia of the nanoneedle.	33
2.6 Proposed Theoretical Model for Implementation of TMT for CR AFM where $w(x, t)$ represents the transverse displacement over time of the model, m is the added mass of the nanoneedle and I_o is the mass moment of inertia of the nanoneedle.	41
2.7 Theoretical Eigensolutions Array Versus delta Array	43
2.8 Theoretical Eigenratio Array Versus delta Array	45
2.9 Theoretical Eigenratio Array Versus delta Array update for non-circular cross section.	54
3.1 Prescribed values for α array [Red Line] versus predicted value for α array [Blue Dots] for the baseline model for the first mode of transverse vibration, where the blue dots not seen on the plot are ignored negative values.	57
3.2 Percent error for the individual predicted values of α for the baseline model for the first mode of transverse vibration, where the cluster of points aligned at 100 percent error are simply a product of a very small predicted value for α compared to a very large prescribed value for α	58
3.3 Prescribed values for α array [Red Line] versus predicted value for α array [Blue Dots] for the baseline model for the second mode of transverse vibration, where the blue dots not seen on the plot are ignored negative values.	59
3.4 Percent error for the individual predicted values of α for the baseline model for the second mode of transverse vibration, where the cluster of points aligned at 100 percent error are simply a product of a very small predicted value for α compared to a very large prescribed value for α	60
3.5 Prescribed values for α array [Red Line] versus predicted value for α array [Blue Dots] for the proposed model for the first mode of transverse vibration, where the blue dots not seen on the plot are ignored negative values.	62
3.6 Percent error for the individual predicted values of α for the proposed model for the first mode of transverse vibrations, where the cluster of points aligned at 100 percent error are simply a product of a very small predicted value for α compared to a very large prescribed value for α	63

Figure	Page
3.7 Prescribed values for α array [Red Line] versus predicted value for α array [Blue Dots] for the proposed model for the second mode of transverse vibration, where the blue dots not seen on the plot are ignored negative values.	64
3.8 Percent error for the individual predicted values of α for the proposed model for the second mode of transverse vibrations, where the cluster of points aligned at 100 percent error are simply a product of a very small predicted value for α compared to a very large prescribed value for α	65
3.9 Prescribed values for α array [Red Line] versus predicted value for α array [Blue Dots] for the updated proposed model for non-circular cross sectional areas for the first mode of transverse vibration, where the blue dots not seen on the plot are ignored negative values.	66
3.10 Percent error for the individual predicted values of α for the proposed model for non-circular cross sectional areas using the information from the first mode of transverse vibration, where the cluster of points aligned at 100 percent error are simply a product of a very small predicted value for α compared to a very large prescribed value for α	67
3.11 Prescribed values for α array [Red Line] versus predicted value for α array [Blue Dots] for the updated proposed model for non-circular cross sectional areas for the second mode of transverse vibrations, where the blue dots not seen on the plot are ignored negative values.	68
3.12 Percent error for the individual predicted values of α for the proposed model for non-circular cross sectional areas from the second mode of vibration, where the cluster of points aligned at 100 percent error are simply a product of a very small predicted value for α compared to a very large prescribed value for α	69
3.13 Percent error for baseline model, proposed model and updated model for predictions of α using data from the first mode of vibration.	70
3.14 Percent error for baseline model, proposed model and updated model for predictions of α using data from the second mode of vibration.	72

1. INTRODUCTION

1.1 Background

Researchers, particularly in the engineering field, are constantly looking for stronger and lighter materials [1], an increase in durability of materials [2], and precise measurements for material properties [3]. The quality of the results obtained during these attempts to improve materials relies directly on the precision of the data and the meticulousness of the procedure. Therefore, in order to obtain an increase in accuracy and detail we must improve the measurement resolution, measurement precision and result interpretation technique, among other factors. Due to the inherently small dimensions of the samples used in nanotechnology, obtaining an increase in accuracy and detail becomes a challenge. Therefore, the use of a powerful microscopy technique is desired for nanoscale purposes.

Some of these microscopy techniques include microscopes such as: the Scanning Tunneling Microscope (STM), which uses the tunneling of scattered electrons to characterize and image a sample's surface and composition for conductive and semi-conductive materials [4], the Transmission Electron Microscope (TEM), which uses the beaming of transmitted electrons in order to characterize internal composition of a sample such as morphology, crystallization, stress and even magnetic domains [5], and the Atomic Force Microscope (AFM), whose operating principle is similar to the STM, but is not limited to the characterization of conductive and semi-conductive materials, since the AFM can also be used for the characterization of non-conductive materials [6].

One of the many advantages provided by these imaging techniques is the possibility of examining a sample's structure and manipulating it in order to achieve a desired change in value for material properties [7]. While material property control and versatility is only one of the many focuses in the field of nanotechnology, the applications range from electronics and renewable energy [8], to medicine and health care [9]. The ability to retrieve atomic surface imaging provides a window to observe the atomic spatial configuration and continue the development and advancement of nanotechnology. The need for a more detailed inspection beyond what optical microscopy can provide becomes evident when examining samples of this nature. This detailed inspection is achieved through means of a sample interaction technique rather than an optical technique. This is how the Atomic Force Microscope is able to examine samples at the nanoscale. Nanoscale refers to samples that are a billionth of a meter in size. This is the length scale where intermolecular forces and quantum effects can be observed. [10]. A popular comparison to put the nanoscale into perspective is that the size of an atom relative to an apple is similar to the size of an apple relative to planet earth.

1.2 Introduction to Non-optical Microscopy:

Atomic Force Microscopy and The Scanning Tunneling Microscope

The Atomic Force Microscope (AFM) was developed in 1985, four years after the development of the noble prize winning Scanning Tunneling Microscope (STM). Gerd Binnig is accredited for the development of the AFM and the STM. Both the AFM and the STM are non-optical microscopes, meaning they do not use the combination of light or beam irradiation and a lens in order to examine or see the sample. The incentive behind non-optical microscopy is that it does not encounter the same spatial resolution limitation that the traditional optical microscopes encounter.

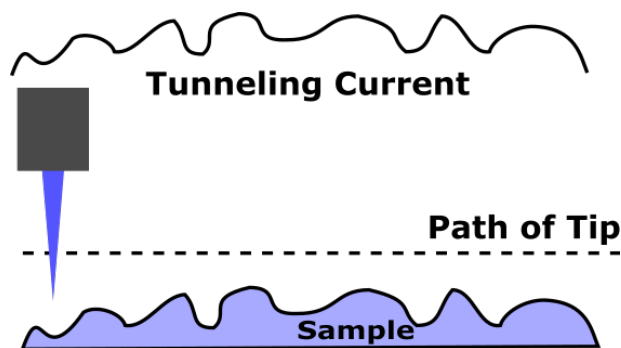


Fig. 1.1. STM Constant Height Mode, showing constant path of tip [dotted line] and varying current values [solid line].

Optical microscopy inherently has a limited spatial resolution due to the diffraction and aberration phenomena involved when dealing with the optical spectrum. This means that the resolution for an optical microscope is limited to half the wavelength of the type of light being utilized. This is known as the Nyquist criterion and it requires a sampling interval equal to twice the highest spatial frequency of the sample in order to accurately preserve the spatial resolution of the image [11]. Non-optical microscopes such as the STM and the AFM use sample interaction techniques in order to retrieve sample imaging. These techniques involve using methods other than the traditional approach, in order to overcome the inherent limitation of the optical microscope.

The AFM's predecessor, the STM, utilizes an electron tunneling technique in order to track the height profile of a sample. This is achieved by incorporating a bias voltage between a conductive sample and a conductive tip probe [4]. When the tip and the sample are brought 10 angstroms apart, which is one nanometer, electrons engage in the tunneling transport behavior, creating current between the sample and tip. Once the tunneling is established, the resulting current varies linearly with tip-to-sample spacing. This is how the STM performs as a high sensitivity non-optical microscope. For property characterization, we can scan the sample and observe the change in tunneling current while maintaining a constant height on the conductive

tip as seen in Figure 1.1. This allows us to characterize the conductivity properties of the sample by creating a mapping based on the tunneling current data and the location of the conductive tip on the sample. For surface imaging purposes we can set the STM to constant current mode, as seen in Figure 1.2, where the conductive tip moves along the height profile of the sample by adjusting position in the vertical direction (further or closer to the sample) in order to maintain constant current.

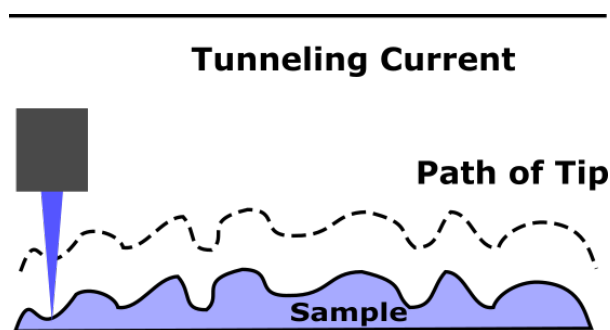


Fig. 1.2. STM Constant Current Mode, showing the path of the tip following the contour of the sample surface with constant tunneling current.

Unfortunately, the STM requires conductive or semi-conductive material in order for the scanning or property characterization to occur. Thanks to the work of Binnig et al., the AFM was able to provide a solution for the imaging of non-conductive materials. The AFM works using a similar principle as the STM, but instead of utilizing currents and voltages, the AFM utilizes nanoforces and nanoscale deflections. The probe of the AFM initially consisted of a tiny strip of gold foil that resembled a microcantilevered beam with a diamond shard at the end. For the most part, these microcantilevered beams and the tip at the end are manufactured out of silicon or silicon nitride. Similar to the STM, the AFM can track the height profile of a sample with a tip-like probe located at the end of a microcantilevered beam. The AFM

can retrieve the height profile by scanning a sample and providing a constant force between the tip and the sample in order to maintain a constant deflection. This is similar to the constant current mode, where the tip adjusts moving up and down the contour of the sample in order to maintain a constant current. The AFM can also operate at a constant height mode, like the STM. The constant height mode for the AFM results in the measure of the change in nanonewton forces between the tip and the sample, which can be used for characterization for mechanical properties of the material, through similar ideas and concepts behind nanoindentation [12].

The AFM probe is used to scan a sample's surface and retrieve the height profile by tracking the deflections of the microcantilevered beam. The height profile is recorded by using a beam-bouncing technique. This technique consists of bouncing a superluminescent diode off the back of a reflective microcantilevered beam into a mirror, which is then reflected into a photodiode that tracks the deflections of the beam [13] [14]. The microcantilevered beam deflections are tracked by feeding the photodiode's data (current position) into a feedback control loop, which compensates for the change in deflection caused by the bumps or depressions of the sample's surface. By adjusting the AFM probe closer or further away from the sample's surface, the AFM maintains and returns to the original deflection. This is known as the constant-force mode and it is used to retrieve three-dimensional topological images of a sample's surface by using the height-profile technique previously described.

The AFM can also be operated at a constant height mode as previously mentioned, where the microcantilevered probe scans while maintaining a constant height. In this mode, the AFM can measure the nanonewton forces between the sample and the tip. These forces vary depending on the distance of the probe and the sample, similar to how the current varies with respect to the distance for the STM. As the probe gets closer to the sample, without making contact, the forces experienced between

the tip and the sample are the attractive van der Waals atomic forces. As soon as the probe and the sample make contact, the forces are now net-repulsive, where the force applied by the tip on the sample is the same force the surface applies back on to the tip. Constant force mode and constant height mode were the two primary modes of AFM when it was first developed in the middle of the 80's. Since then, multiple modes of AFM have been developed and are widely used to predict material properties and acquire surface imaging of challenging samples of biological nature [15]. The mode of the AFM can be chosen in order to tailor the experimental procedure to the requirements of the sample, or to predict material properties, such as Young's modulus of elasticity. The property retrieval modes involve the implementation of computational techniques along with a theoretical mathematical model in order to retrieve these properties. These techniques utilize various data acquired by the AFM and output the values for the desired material properties of the sample. The AFM is a powerful instrument and can be utilized in various ways to provide a window to closely observe the sample and characterize mechanical properties of samples through different modes of operation.

1.3 Force Response and Modes of AFM

Originally, the AFM's purpose was to provide a topological image at an atomic level for non-conductive materials. It was not until later that researchers began to implement different experimental techniques and modes of AFM to retrieve material properties. Contact Resonance Atomic Force Microscopy (CR AFM) is one of these techniques and will be discussed in greater depth in the CR AFM section [16] [17].

The different modes of operation for an AFM still work behind the primary force-displacement relationships the original modes of AFM possess. The differences between these modes are characterized by the force-interaction the sample and the

AFM probe experience. In the previous section, we briefly described the constant-force mode of operation for the AFM. This mode of AFM falls under the category of Contact mode of AFM. During this mode, the forces experienced between the AFM probe and the sample are due to the Coulomb electrostatic interactions happening when the AFM probe and the sample make contact. This contact and interaction follows Coulomb's Law and results in net electrostatic repulsive forces. Meaning, these electrostatic forces are equal and opposite in direction and magnitude, respectively. The response for the AFM's microcantilevered beam while in net-repulsive contact can be observed in Figure 1.3 and a graph of the force-displacement relationship can be observed in Figure 1.5

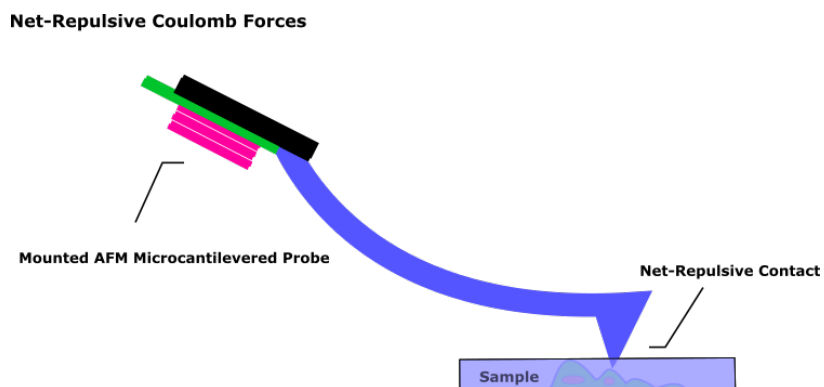


Fig. 1.3. Mounted microcantilevered beam in net-repulsive contact with the sample.

The procedure for the Contact mode begins by pressing the microcantilevered beam against the sample's surface by means of a lead zirconate titanate (PZT) element, in order to obtain a deflection. This PZT element functions as an actuator that can transform electrical energy into mechanical energy. This translates into a motion in the vertical direction (further or closer away from the sample) in order to obtain a deflection. This deflection is a direct result of the net-repulsive contact discussed earlier, meaning that the force experienced by the sample from the AFM probe is the same force experienced by the AFM probe from the sample. This is

known as repulsive regime and can be observed in Figure 1.5. The AFM probe then scans the sample's surface while remaining in net-repulsive contact with the sample. While in contact mode, the deflection of the microcantilevered beam is tracked and compared in a feedback control system to the original desired value of deflection. If there is a change in deflection, the feedback control uses an amplifier to apply a voltage, adjusting the probe in the vertical direction in order to maintain the desired deflection. This provides the height profile of the sample. A downfall of the contact mode is the wear and tear of the probe. This leads to dulling of the tip and causes a lower image resolution due to the lower sensitivity to bumps and depressions of the surface. Unfortunately, Contact mode can be a destructive procedure for the sample as well. If we are scanning a sample that is much softer than the stiffness of the microcantilevered AFM probe, the probe would essentially destroy the sample. In this case, we are limited by the stiffness of the sample and the available stiffness of the microcantilevered AFM probe. Therefore, in cases where contact must be avoided, a Non-contact mode becomes a better alternative.

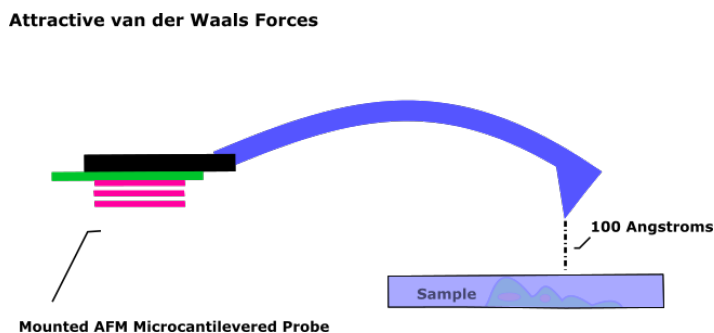


Fig. 1.4. Mounted microcantilevered beam in attractive regime with the sample due to van der Waals forces.

The Non-contact mode involves the use of the attractive van der Waals forces between the tip and the sample, rather than the net-repulsive contact forces. These are the forces the sample and the tip experience when they are 50 to 150 Angstroms away

from each other. The van der Waals force-interaction results in the opposite response by the AFM probe, compared to the Coulomb force-interaction. This response can be observed in Figure 1.4 and a graph of the force-displacement relationship can be observed in Figure 1.5. At this distance, the tip and the sample are no longer in contact. The van der Waals forces are significantly weaker than the forces experienced in Contact mode, so the microcantilevered beam is given a small oscillation in order to detect these small forces through changes in amplitude and frequency. This mode of AFM becomes a good alternative to scanning softer samples, but even with the addition of the small oscillations, the magnitude of the van der Waals forces still presents a challenge. Therefore, the development of an intermittent mode of AFM was implemented in order to overcome this obstacle. This third mode of AFM is a combination of the Contact mode and Non-contact mode. Intermittent-contact mode of AFM, also known as Tapping mode, was developed as a better alternative to the Non-contact mode for the scanning of biological soft samples. This mode of AFM was first implemented by Putnam et al., where they measured the frequency response and the tip-sample distance curves both in air and liquid [18].

The tapping mode is a technique which allows for topological imaging of soft samples that can be damaged with ease. In the tapping mode, the AFM probe comes into contact with the sample, resulting in a net-repulsive Coulomb force-interaction. The tip then lifts off the sample, moving to the next location and comes into contact again resulting in a net-repulsive Coulomb force-interaction. This repetitive motion results in a “tapping” of the probe across the sample. This is achieved by sinusoidally exciting the microcantilevered beam near resonance by means of the PZT element, similar to the Non-contact mode. By tracking the shift in amplitude of the oscillations, we can obtain a height profile based on the bumps and depressions of the sample. When there is a bump, the probe has less space to oscillate, resulting in a decrease

in amplitude. When there is a depression, the probe has more space to oscillate, resulting in an increase in amplitude. The net force response of the microcantilevered beam can be observed in Figure 1.5 and is a combination of the van der Waals and the Coulomb behaviors. Here it is important to notice the force response by the microcantilevered beam when coming in and out of contact. The nonlinear behavior of the forces provides challenges and obstacles in the implementation of theoretical mathematical models for property retrieval modes of AFM.

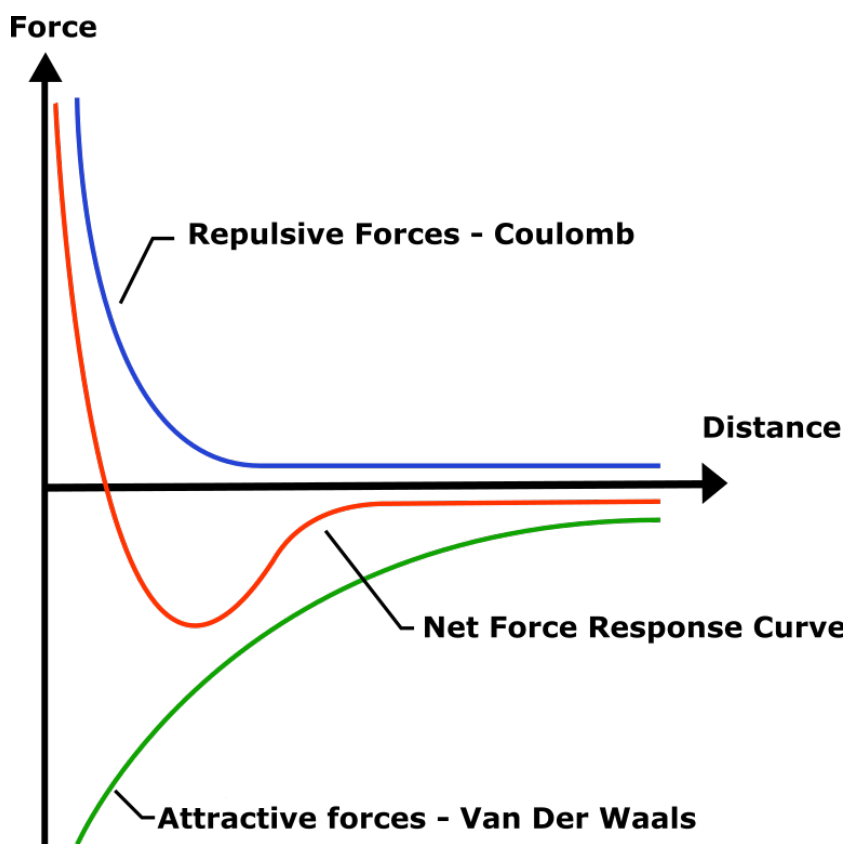


Fig. 1.5. Force Curve Response for the microcantilevered beam compared to the van der Waals and Coulomb interactions

For the scanning of biological samples, most of these samples need to be in their native environment. For the vast majority of these samples, this means a liquid environment. Therefore, if any mode of AFM that uses resonance of the probe was to

be utilized, the microcantilevered beam would need to oscillate while submerged in a liquid. Unfortunately, in this mode of AFM, the oscillation amplitude of the microcantilevered beam lacks sensitivity to the small shifts of frequency while submerged in liquid [19]. This is due to the considerable effect that viscosity of the fluid has on the response of the microcantilevered beam [20]. The presence of hydrodynamic forces from the liquid on the microcantilevered beam have great effect on the response of the beam. Therefore, due to the complexity of these hydrodynamic forces, it becomes a challenge to model and incorporate them. The liquid environment limits our ability to retrieve the true values for the natural frequencies of the probe while it oscillates. In this mode, we heavily rely on the ability to use the frequency spectral data to our advantage, therefore the presence of the liquid environment tampers with our modeling and data retrieval.

In the absence of liquid environment, modal analysis for the microcantilevered beam is routine, and therefore can be done through multiple techniques, since the relationship between displacement-forces and frequency-amplitudes remains linear. This is no longer the case when performing the same rigorous analysis in a liquid environment. The main effects observed for the frequency response are a decrease in amplitude of vibration, due to an increase in damping from the liquid environment, and a decrease in resonant frequency, due to the added mass effect, which is also a result of the liquid environment. The added mass effect is a consequence of the density of the fluid. Increasing the liquid density causes an increase in vibration amplitude, meanwhile the natural frequency reduces [19]. The viscosity of the liquid has a direct effect on the damping coefficient and decreases the amplitude of vibration, as previously mentioned. Differing from the density, although the amplitude changes for the viscosity effect, the natural frequency remains constant. All of these factors result in a reduction of resolution when performing frequency scans, which in turn

results in blurrier images. In order to overcome these challenges Minary et al. have developed a mode of AFM called the Trolling Mode, which addresses the increase of damping and the presence of hydrodynamic damping forces.

1.4 Trolling Mode

As previously mentioned, there are multiple challenges involved when using tapping mode in a liquid environment. The main obstacles being the loss of image resolution and the presence of the hydrodynamic damping forces. The increase of damping caused by the liquid environment translates in a decrease of Quality Factor (Q-Factor). The Q-Factor is used to describe levels of damping of an AFM probe. Higher damping results in lower Q-Factors, and lower Q-Factors result in blurrier images. Research has been performed in regards to the reconstruction of the hydrodynamic forces [21], but the loss of image resolution and intrinsically low Q-Factors is a product of the liquid environment. In 2012, Minary et al. [22] developed a technique to overcome these challenges. This technique is known as the Trolling Mode Technique (TMT) and consists of modifying the experimental setup in order to remove the probe from the liquid environment while still being able to scan the sample's surface. The micro-cantilevered probe is modified to include a 60 micrometer long chromium needle with a radius of 300 nanometers, as depicted in Figure 1.6.

This results in the removal of the probe body from the liquid environment. The probe is now free to oscillate without the presence of hydrodynamic damping forces (negligible for air). This also results in an increase of Q-Factor (Lower damping), which provides a sharper resolution criteria for frequency data acquisition, leading to sharper imaging. The TMT was developed for the use of AFM on biological samples, but can be extended to any type of sample in a liquid environment. The TMT experimental setup was designed for and intended to be used with the previously

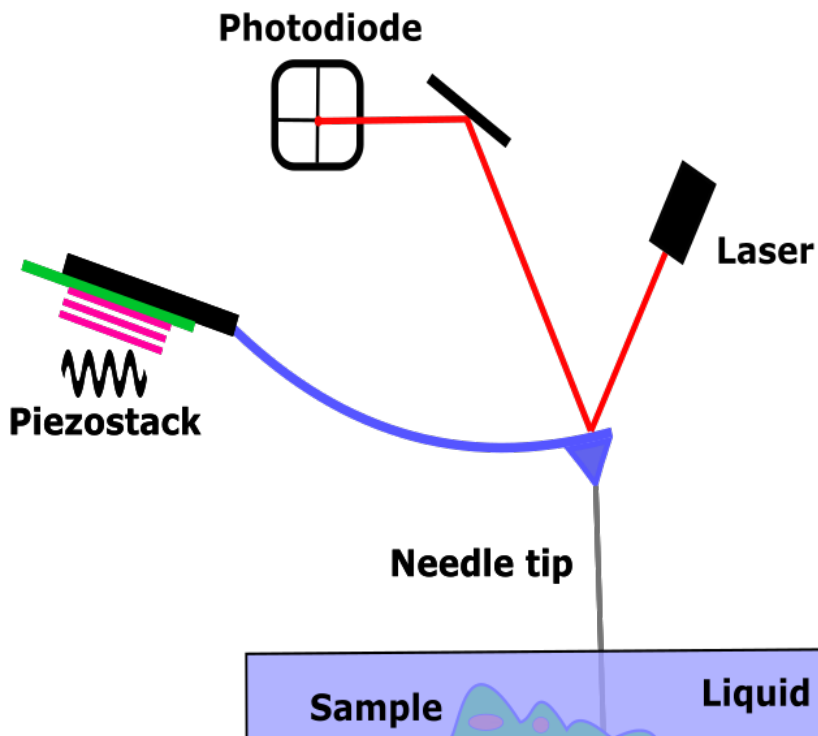


Fig. 1.6. Trolling Mode Technique experimental setup with piezo stack element, photodiode, needle tip and submerged sample.

introduced AFM Tapping Mode. As previously mentioned, the Tapping Mode of AFM consists of the AFM probe cycling between contact and non-contact phases. This results, as suggested by the name, in a tapping motion by the probe on the sample. The soft nature of biological samples requires us to be extremely careful when performing AFM scans in order to avoid damage or destruction of the sample. For this reason, the AFM Tapping Mode is a good candidate for the scanning of biological samples. Since the probe comes in and out of contact before moving to the next location on the sample, the integrity of the sample is better preserved. It is important to mention that the same advantage the Tapping Mode possesses is also a disadvantage. If we refer back to Figure 1.5 from the previous section, we observe a constant cycling between linear and non-linear forces at the time of our scan, thus

providing a challenge for any modeling or predictions to be made in regards to material properties. In order to further extend this research, we implement the Trolling Mode Technique with a property retrieval AFM mode known as Contact Resonance.

1.5 Contact Resonance Atomic Force Microscopy: The Theoretical Model

Contact Resonance (CR) atomic force microscopy (AFM) is a relatively new, popular measurement technique used to characterize nanoscale material properties. CR AFM has been used to characterize the properties of thin metallic films [23] and polymer blends [24]. In order to retrieve these material properties, the microcantilevered AFM probe is excited near resonance while in permanent, net-repulsive contact with the sample of interest. The resulting vibrations between the AFM probe and the sample are denoted as the coupled vibrations or in-contact frequencies. Once we've recorded the value for the in-contact vibration, we remove the AFM probe from net-repulsive contact with the sample and excite it near resonance while it is "free", or not in contact with the sample, this is known as the free vibrations. The permanent, net-repulsive coupled vibrations and the free vibrations are then utilized in order to retrieve a material's mechanical property. We accomplish this by implementing a mathematical model which represents the microcantilevered AFM probe and the sample interaction. Once we input these vibrations into the mathematical model, it can output material properties, such as Young's modulus of elasticity.

In order to retrieve accurate nanoscale material properties, the mathematical model must closely resemble the physical parameters of the AFM microcantilevered probe. The theoretical model is a mathematical representation of the spatial and temporal behavior of the probe. Therefore, when utilizing the CR AFM technique, the mathematical model must be tailored to the experimental setup being used by

paying close attention to the geometrical and natural boundary conditions of the system.

In order to derive the theoretical model, we use the Euler-Bernoulli (EB) beam theory, which we will discuss in greater depth in the Theoretical Modeling section, as well as the parameters to consider when deriving this model. A traditional theoretical CR AFM model for the retrieval of Young's modulus of elasticity can be seen in Figure 1.7

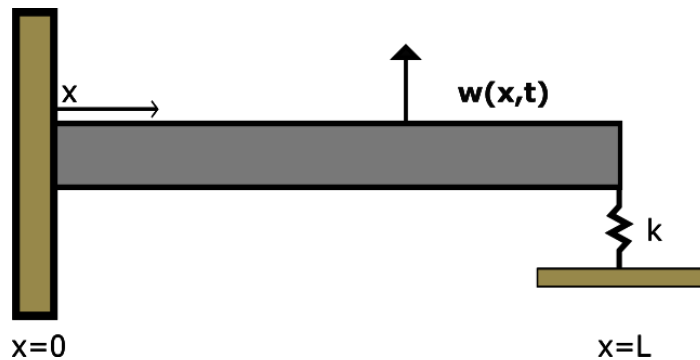


Fig. 1.7. Euler-Bernoulli Beam Baseline Theoretical Model for CR AFM Young's modulus retrieval technique, where $w(x,t)$ represents the transverse displacement over time of the model and k is the stiffness coefficient for the spring.

For property prediction purposes, if Young's modulus of elasticity is what we are interested in, modeling the interaction with a single spring is sufficient [25]. The addition of a damper to the model allows for retrieval of viscoelastic properties of the sample, but also adds complexity to the procedure and requires more computational power. The spring and the damper are used to model the contact interaction which occurs between the tip and the sample. The spring and damper's configuration will have an effect on the obtained results. There is vast research in the contact mechanics modeling, but for the purpose of this research, we will focus on modeling the dynamics of the microcantilevered probe and the tip. The correlation between the varying

geometries of the probe and the theoretical model is our main focus throughout this document. Close attention should be paid to the physical dimensions and aspects of any features on the microcantilever probe, such as variations in size, location and geometry of the tip and body of the probe, when deriving the theoretical model in order to predict valuable data. The accuracy of the theoretical model relies on how well the model's physical parameters are represented and implemented into the mathematical equivalent model. Since the probe is the interface for the sample, the values retrieved from the model will not provide meaningful data unless the development of the model and numerical techniques involved are performed with diligence.

For most traditional setups, the AFM probe may consist of a 200 micrometer long, 30 micrometer wide and 2 micrometer thick silicon cantilever with a small pyramid-like tip located at the end. This tip can vary in size, but for the baseline model, the mass of the tip is neglected, since it is usually much smaller compared to the beam. For the purposes of this research, we focus on the tailoring of the baseline theoretical model for a non-traditional AFM setup developed in 2012 by Minary et al., the Trolling Mode Technique (TMT). By tailoring this theoretical model for TMT, we then implement it with the CR AFM technique for material property retrieval. In order to tailor our theoretical model for the TMT, rigorous analyses of the effect that the three-dimensional tip has on the system dynamics are needed. Throughout the following section, we analyze the full three-dimensional geometry of AFM cantilever probes with long, heavy tips to determine their effect on the surface coupled vibrations of the system. The derivation for the theoretical model and parameter calibration technique for the TMT is also presented in the following section.

2. TROLLING MODE: A CONTACT RESONANCE APPROACH

2.1 3D Finite Element Model

In order to retrieve experimental data, we create a 3D finite element model and perform a modal analysis to reveal the values and shapes of the natural frequencies and modes of vibration. In order to conduct this modal analysis, the computer software uses a subdivision technique resulting in the creation of points throughout the model, these points are denoted as nodes. The location of these nodes with respect to each other is used by the computer software in order to perform a variety of simulations. In this case, as previously mentioned, we perform a modal analysis, where we are interested particularly in the natural frequencies of the model. The existence and distribution of these nodes on the model plus the resulting subdivisions make up the model's mesh. As more nodes are added, the mesh becomes finer and it more accurately represents the model. In order to validate our model, we use the manipulation of this mesh to reach convergence. This involves subdividing the model until further subdivision of the model will not cause a significant change in the values retrieved from our modal analysis, i.e. 50 subdivisions in the y -direction (from Figure 2.1) is the amount of subdivisions required for convergence. Meaning, if we ran our modal analysis various times for multiple subdivisions in the y -direction, we would see a change in the values of the natural frequencies retrieved every time we changed the number of subdivisions. Once we reach the convergence value, we no longer would observe a significant change in the value of the frequencies retrieved.

In this case we present our 3D finite element model for the TMT, with dimensions and material properties, as well as the convergence analysis on our model. It is extremely important to ensure we reach convergence for our model, since we will be using it to verify the theoretical model proposed. Figure 2.1 shows our 3D model while engaged in its third mode of vibration for transverse oscillations. Our 3D model

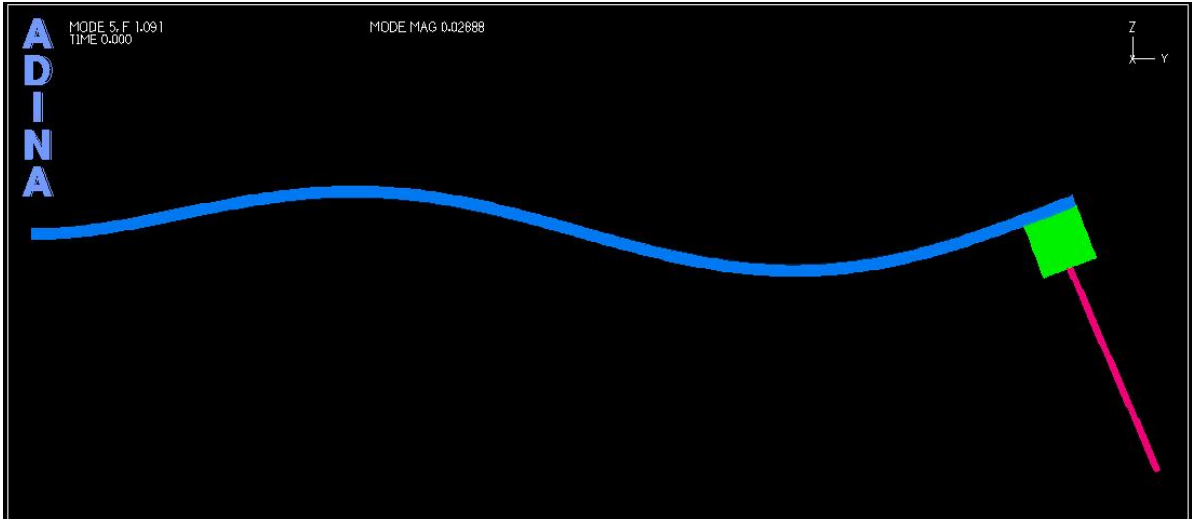


Fig. 2.1. 3D Finite Computer Model for TMT Experimental Setup in the third mode of transverse vibration.

consists of a parallelepiped that extends $200 \mu\text{m}$ long and $30 \mu\text{m}$ wide at $2 \mu\text{m}$. Our model is fixed at one end, meaning it cannot displace or rotate in any direction. At the other end we have the mounting tip which is modeled as a cube of $10 \mu\text{m}$ in height, width and length. There is a long tip located at the center of the mounting tip: this represents the nanoneedle used in the TMT. In our 3D model the length of the nanoneedle is $39 \mu\text{m}$ with a width of $1.25 \mu\text{m}$ at $1 \mu\text{m}$ thickness. At the tip of the needle we have placed 5 linear single degree of freedom springs, one at each corner of the cross sectional area and one at the center of the cross sectional area. We use the springs in our model in order to represent the tip-sample interaction that occurs

when the AFM and the sample are in contact. Figure 2.2 shows the mesh for our 3D model while engaged in the second mode of vibration for transverse oscillations while in contact with a low stiffness spring. We use the material properties for silicon for the

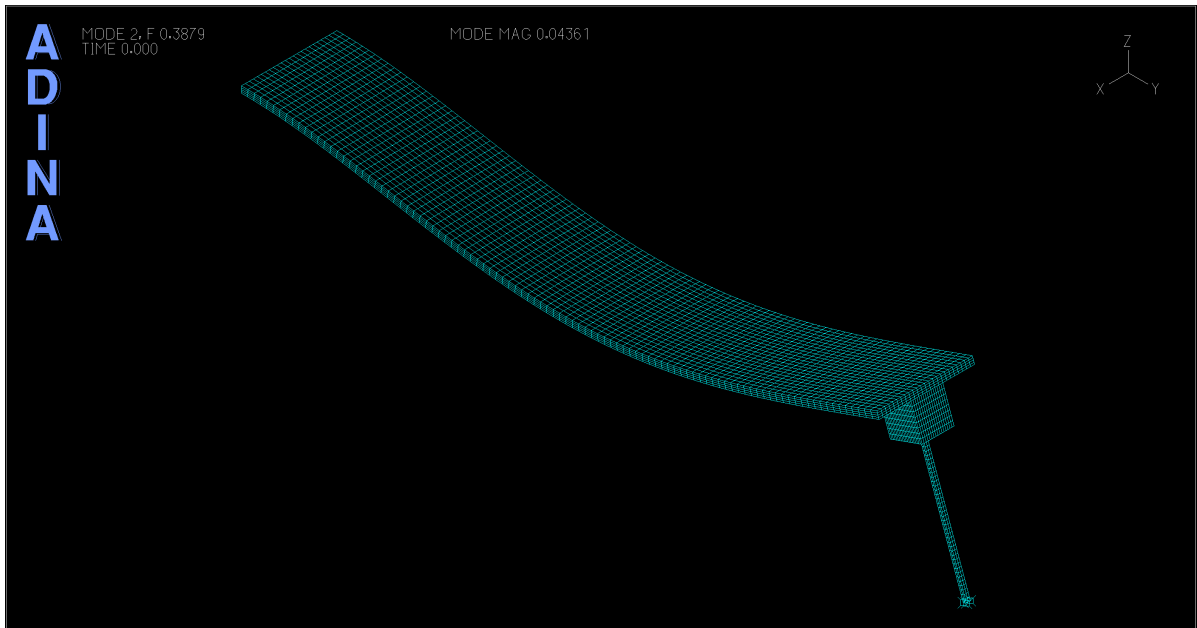


Fig. 2.2. 3D Finite Computer Model for TMT Experimental Setup in the third mode of transverse vibration.

beam in the 3D model and the material properties for chromium for the nanoneedle. The 5 springs are varied equally for simulation purposes by creating an array for values of α that are equally spaced apart based on the logscale. In the application of the theoretical model these five springs are modeled and reduced to one equivalent spring. The spring represents the interface interaction between the tip and the sample, thus providing us with a way to characterize the stiffness sample. As mentioned before, the use of CR AFM involves the implementation of a theoretical mathematical model in order to retrieve material properties. This theoretical model must accurately represent the physical model. In this case the physical model is our 3D finite element model. The data we input into our theoretical model will be retrieved from the modal

analysis performed on the 3D model. In the next section we present the derivation of the theoretical model, where great detail is to be paid to the model's geometry. In order to capture the dynamics of the added long tip, the following technique is used.

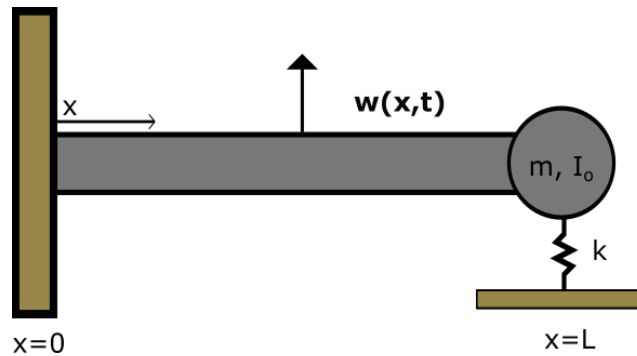


Fig. 2.3. Proposed Theoretical Model for Implementation of TMT for CR AFM where $w(x,t)$ represents the transverse displacement over time of the model, k is the stiffness coefficient for the spring, m is the added mass of the nanoneedle and I_o is the mass moment of inertia of the nanoneedle.

2.2 Euler-Bernoulli Beam Model

In order to capture the dynamic behavior of the model, we define the natural and geometric boundary conditions of the system. These conditions rule our model's dynamic behavior and include the presence of features such as the long added tip at the end of the microcantilevered beam. A common boundary condition is the fixed condition, meaning that at one end the microcantilevered beam is fixed and cannot displace in any direction. These boundary conditions dictate the response of the model and divide into two categories, geometric and natural. The geometric boundary conditions describe the displacement and slope relationship at either end of the microcantilevered beam. The natural boundary conditions describe the force

and moment relationship at either end of the microcantilevered beam. In this case, at $x = 0$ from Figure 2.3, we can observe a fixed boundary condition, meaning the displacement and slope will be zero at that location. So, at $x = 0$ our model is governed by geometrical boundary conditions. At $x = L$, the dynamics of the cantilever are governed by the nanoneedle. The nanoneedle is the tip of the probe during the AFM scanning. Therefore, it interacts with the surface and this interaction is modeled as a spring. The surface interaction model can vary as mentioned before, but for our interest in the retrieval of the Young's Modulus, a single spring is required. In order to capture the dynamics of the nanoneedle, a force-balance and moment-balance relationship must be derived. In this case, we consider an added mass effect due to the mass of the nanoneedle and an added inertia effect due to the long tip. These are the boundary conditions that will be implemented into the theoretical model and result in a mathematical representation of the model.

We begin the derivation from the Euler-Bernoulli beam equation for Free Vibrations [26].

$$c^2 \frac{\partial^4 w}{\partial x^4}(x, t) + \frac{\partial^2 w}{\partial t^2}(x, t) = 0, \quad (2.1)$$

where

$$c = \sqrt{\frac{EI}{\rho A}}. \quad (2.2)$$

In Equation 2.2, E is the Young's modulus, I is the area moment of inertia, ρ is the density, and A is the cross sectional area. The solution to the fourth order Euler-Bernoulli equation can be found using the method of separation of variables, which assumes:

$$w(x, t) = W(x)T(t), \quad (2.3)$$

where $W(x)$, is the spatial solution for Equation 2.1 and $T(t)$ is the temporal solution for Equation 2.1. These two solutions combined describe the total response for our system in the time and space domain. Meaning they provide the exact shape our model is currently experiencing at any given point in time. By substituting the relationship in Equation 2.43 into Equation 2.3 we obtain

$$\frac{c^2}{W(x)} \frac{d^4W(x)}{dx^4} = -\frac{1}{T(t)} \frac{d^2T(t)}{dt^2} = \omega^2, \quad (2.4)$$

where ω^2 is a positive constant. Equation 2.4 can be written as two separate equations:

$$\frac{d^4W(x)}{dx^4} - \beta^4W(x) = 0 \quad (2.5)$$

and

$$\frac{d^2T(t)}{dt^2} + \omega^2T(t) = 0, \quad (2.6)$$

where

$$\beta^4 = \frac{\omega^2}{c^2} = \frac{\rho A \omega^2}{EI}. \quad (2.7)$$

The solution for equation 2.5 is found by assuming

$$W(x) = Ce^{sx}, \quad (2.8)$$

where C and s are constants. This gives an auxiliary equation of

$$s^4 - \beta^4 = 0, \quad (2.9)$$

which has roots $s_{1,2} = \pm\beta$ and $s_{3,4} = \pm i\beta$. This gives the solution

$$W(x) = Ae^{\beta x} + Be^{-\beta x} + Ce^{i\beta x} + De^{-i\beta x}. \quad (2.10)$$

The solution can then be written as

$$W(x) = C_1 \cos(\beta x) + C_2 \sin(\beta x) + C_3 \cosh(\beta x) + C_4 \sinh(\beta x), \quad (2.11)$$

where $W(x)$ is the transverse deflection shape of the beam at a given location x , β is the eigenvalue, and C_1, C_2, C_3 , and C_4 are constants that are determined by the beam's boundary conditions [26].

Now, we must enforce our previously discussed boundary conditions. First we translate them into their mathematical equivalent. For our displacement boundary condition at $x = 0$, we have

$$w(0, t) = 0. \quad (2.12)$$

For our slope boundary condition at $x = 0$

$$\frac{\partial w(0, t)}{\partial x} = 0. \quad (2.13)$$

For our moment balance boundary condition at $x = L$

$$EI \frac{\partial^2 w(L, t)}{\partial x^2} = I_o \frac{\partial^3 w(L, t)}{\partial x \partial t^2}, \quad (2.14)$$

and for our force balance boundary condition at $x = L$, we have

$$EI \frac{\partial^3 w(L, t)}{\partial x^3} = m \ddot{w}(L, t) + kw(L, t). \quad (2.15)$$

We have represented the needle's dynamics through the added mass effect and the rotational inertia effect, but we are not modeling the pinned condition that occurs while the needle is in contact with the sample, nor the flexural rigidity of the needle. These are higher fidelity parameters to be updated in order to improve the model.

Once the boundary conditions are defined, we implement our fixed geometrical boundary condition to reduce our spatial solution in Equation 2.11. It can be helpful to enforce the geometrical boundary conditions of the model before the natural boundary conditions. This is due to the typical reduction of the spatial solution that occurs with a fixed boundary condition. In this case, both conditions Equation 2.12 and Equation 2.13 result in

$$C_1 = -C_3$$

and

$$C_2 = -C_4$$

for Equation 2.11. This leads to a reduced spatial solution of

$$W(x) = C_1(\cos(\beta x) - \cosh(\beta x)) + C_2(\sin(\beta x) - \sinh(\beta x)). \quad (2.16)$$

Once we have reduced our spatial solution with our geometrical boundary conditions, we enforce the natural boundary conditions, Equations 2.14 and 2.15.

We then substitute Equation 2.16 into the moment boundary condition, Equation 2.14, thus obtaining the following equation

$$\begin{aligned} EI\beta^2(C_1[-\cos(\beta L) - \cosh(\beta L)] + C_2[-\sin(\beta L) - \sinh(\beta L)])T(t) = \\ - I_o\omega^2\beta T(t)(C_1[-\sin(\beta L) - \sinh(\beta L)] + C_2[\cos(\beta L) - \cosh(\beta L)]), \end{aligned} \quad (2.17)$$

We further expand by using the relation in Equation 2.7

$$w^2 = (\beta L)^4 \frac{EI}{\rho AL^4}. \quad (2.18)$$

Substituting back into Equation 2.17, dividing by EI and dividing by $T(t)$ we obtain

$$\begin{aligned} & \beta^2(C_1[-\cos(\beta L) - \cosh(\beta L)] + C_2[-\sin(\beta L) - \sinh(\beta L)]) = \\ & - I_o(\beta L)^4 \frac{EI}{\rho AL^4} \beta (C_1[-\sin(\beta L) - \sinh(\beta L)] + C_2[\cos(\beta L) - \cosh(\beta L)]). \end{aligned} \quad (2.19)$$

In order for this mathematical model to remain as a non-dimensional model, it must be able to provide eigenvalue solutions of β for a beam of any given length. Therefore we must keep our solution in terms of βL by multiplying both sides of the equation by L^2 .

$$\begin{aligned} & (\beta L)^2(C_1[-\cos(\beta L) - \cosh(\beta L)] + C_2[-\sin(\beta L) - \sinh(\beta L)]) = \\ & - I_o(\beta L)^5 \frac{EI}{\rho AL^3} (C_1[-\sin(\beta L) - \sinh(\beta L)] + C_2[\cos(\beta L) - \cosh(\beta L)]), \end{aligned} \quad (2.20)$$

We introduce the non-dimensional parameter, \hat{I} , which is used to describe the ratio between the mass moment of inertia for the added mass and the mass moment of inertia for the beam

$$\hat{I} = \frac{I_o}{\rho AL^3}. \quad (2.21)$$

Therefore, by substituting Equation 2.21 into our final expression and dividing by $(\beta L)^2$, the moment natural boundary condition is

$$\begin{aligned} & \hat{I}(\beta L)^3(C_1[-\sin(\beta L) - \sinh(\beta L)] + C_2[\cos(\beta L) - \cosh(\beta L)]) + \\ & (C_1[-\cos(\beta L) - \cosh(\beta L)] + C_2[-\sin(\beta L) - \sinh(\beta L)]) = 0, \end{aligned} \quad (2.22)$$

We now use a similar procedure for Equation 2.15, the force natural boundary condition.

$$\begin{aligned}
EI\beta^3(C_1[\sin(\beta L) - \sinh(\beta L)] + C_2[-\cos(\beta L) - \cosh(\beta L)])T(t) = \\
- m\omega^2 T(t)(C_1[\cos(\beta L) - \cosh(\beta L)] + C_2[\sin(\beta L) - \sinh(\beta L)]) \\
+ kT(t)(C_1[\cos(\beta L) - \cosh(\beta L)] + C_2[\sin(\beta L) - \sinh(\beta L)]), \quad (2.23)
\end{aligned}$$

Substituting Equation 2.18, dividing by $T(t)$ and EI , and multiplying by L^3 in order to maintain solutions of βL , we obtain

$$\begin{aligned}
(\beta L)^3(C_1[\sin(\beta L) - \sinh(\beta L)] + C_2[-\cos(\beta L) - \cosh(\beta L)]) = \\
- \frac{m}{\rho AL}(\beta L)^4(C_1[\cos(\beta L) - \cosh(\beta L)] + C_2[\sin(\beta L) - \sinh(\beta L)]) \\
+ \frac{kL^3}{EI}(C_1[\cos(\beta L) - \cosh(\beta L)] + C_2[\sin(\beta L) - \sinh(\beta L)]). \quad (2.24)
\end{aligned}$$

We introduce the non-dimensional parameter Δ which represents the mass ratio between the added mass and the beam.

$$\Delta = \frac{m}{\rho AL}. \quad (2.25)$$

Therefore, we can further simplify Equation 2.24 into

$$\begin{aligned}
(\beta L)^3(C_1[\sin(\beta L) - \sinh(\beta L)] + C_2[-\cos(\beta L) - \cosh(\beta L)]) = \\
- \Delta(\beta L)^4(C_1[\cos(\beta L) - \cosh(\beta L)] + C_2[\sin(\beta L) - \sinh(\beta L)]) \\
+ \frac{kL^3}{EI}(C_1[\cos(\beta L) - \cosh(\beta L)] + C_2[\sin(\beta L) - \sinh(\beta L)]). \quad (2.26)
\end{aligned}$$

Lastly, we incorporate the non-dimensional parameter α , which represents the stiffness ratio for the spring and the beam,

$$\alpha = \frac{k}{k_c}, \quad (2.27)$$

where

$$k_c = \frac{3EI}{L^3}. \quad (2.28)$$

Equation 2.28 is the static stiffness of a cantilever beam, modeled as a point-load added at the tip of the beam in a quasi-static fashion. This means that the point-load is applied slow enough for the beam to deform slowly enough to retrieve a low strain rate, this then ensures we can ignore the inertia force due to its small magnitude.

In order to incorporate our Equation 2.27 into Equation 2.26, we observe that the last term on the RHS of Equation 2.26 is,

$$\frac{kL^3}{EI}(C_1[\cos(\beta L) - \cosh(\beta L)] + C_2[\sin(\beta L) - \sinh(\beta L)]). \quad (2.29)$$

Here we observe if we multiply this entire term by $\frac{3}{3}$ we can group our variables in order to incorporate α into our equation resulting in

$$\frac{3kL^3}{3EI}(C_1[\cos(\beta L) - \cosh(\beta L)] + C_2[\sin(\beta L) - \sinh(\beta L)]). \quad (2.30)$$

Where we can observe that Equation 2.30 can then be expressed as

$$\frac{3k}{k_c}(C_1[\cos(\beta L) - \cosh(\beta L)] + C_2[\sin(\beta L) - \sinh(\beta L)]). \quad (2.31)$$

Therefore, we can substitute Equation 2.31 into Equation 2.30 and update our boundary condition, Equation 2.26, thus obtaining

$$\begin{aligned} & \Delta(\beta L)^4(C_1[\cos(\beta L) - \cosh(\beta L)] + C_2[\sin(\beta L) - \sinh(\beta L)]) \\ & + (\beta L)^3(C_1[\sin(\beta L) - \sinh(\beta L)] + C_2[-\cos(\beta L) - \cosh(\beta L)]) \\ & - 3\alpha(C_1[\cos(\beta L) - \cosh(\beta L)] + C_2[\sin(\beta L) - \sinh(\beta L)]) = 0. \end{aligned} \quad (2.32)$$

We can arrange Equation 2.22 and Equation 2.32 into a 2x2 matrix

$$\begin{bmatrix} A_{11} & A_{12} \\ A_{21} & A_{22} \end{bmatrix} [C_n] = 0. \quad (2.33)$$

Where the entries are as follows

$$A_{11} = \hat{I}(\beta L)^3[-\sin(\beta L) - \sinh(\beta L)] + [-\cos(\beta L) - \cosh(\beta L)] \quad (2.34)$$

$$A_{12} = \hat{I}(\beta L)^3[\cos(\beta L) - \cosh(\beta L)] + [-\sin(\beta L) - \sinh(\beta L)], \quad (2.35)$$

$$\begin{aligned} A_{21} = & \Delta(\beta L)^4[\cos(\beta L) - \cosh(\beta L)] + (\beta L)^3[\sin(\beta L) \\ & - \sinh(\beta L)] - 3\alpha[\cos(\beta L) - \cosh(\beta L)], \end{aligned} \quad (2.36)$$

$$\begin{aligned} A_{22} = & \Delta(\beta L)^4[\sin(\beta L) - \sinh(\beta L)] + (\beta L)^3[-\cos(\beta L) \\ & - \cosh(\beta L)] - 3\alpha[\sin(\beta L) - \sinh(\beta L)]. \end{aligned} \quad (2.37)$$

We take the determinant of this matrix and set it equal to zero in order to make sure that the system of homogeneous linear equations represented by our matrix

has a non-trivial solution. Therefore our characteristic equation is transcendental and will always have an infinite number of solutions. The resulting equation from the determinant of the matrix A in Equation 2.33 is known as the Characteristic Equation (Char. Eq.). The solutions to the Char. Eq. are known as the eigenvalues and represent the non-dimensional natural frequencies of the system, in this case, our TMT model. The resulting equation or Char. Eq. for our mathematical model can be seen in Equation 2.38.

$$\begin{aligned}
& -\Delta\hat{I}\sin(\beta L)^2(\beta L)^7 + \Delta\hat{I}\sinh(\beta L)^2(\beta L)^7 - \Delta\hat{I}\cos(\beta L)^2(\beta L)^7 \\
& + 2\Delta\hat{I}\cos(\beta L)\cosh(\beta L)(\beta L)^7 - \Delta\hat{I}\cosh(\beta L)^2(\beta L)^7 + 2\hat{I}\sin(\beta L)\cosh(\beta L)(\beta L)^6 \\
& + 2\hat{I}\sinh(\beta L)\cos(\beta L)(\beta L)^6 - 2\Delta\sin(\beta L)\cosh(\beta L)(\beta L)^4 + 2\Delta\sinh(\beta L)\cos(\beta L)(\beta L)^4 \\
& \quad + 3\hat{I}\sin(\beta L)^2\alpha(\beta L)^3 - 3\hat{I}\sinh(\beta L)^2\alpha(\beta L)^3 + 3\hat{I}\cos(\beta L)^2\alpha(\beta L)^3 \\
& \quad - 6\hat{I}\cos(\beta L)\cosh(\beta L)\alpha(\beta L)^3 + 3\hat{I}\cosh(\beta L)^2\alpha(\beta L)^3 \\
& + \sin(\beta L)^2(\beta L)^3 - \sinh(\beta L)^2(\beta L)^3 + \cos(\beta L)^2(\beta L)^3 + 2\cos(\beta L)\cosh(\beta L)(\beta L)^3 \\
& + \cosh(\beta L)^2(\beta L)^3 + 6\sin(\beta L)\cosh(\beta L)\alpha - 6\sinh(\beta L)\cos(\beta L)\alpha = 0. \quad (2.38)
\end{aligned}$$

Therefore the proposed model can be expressed as

$$f(\beta_n L, \hat{I}, \Delta, \alpha) = 0 \quad (2.39)$$

Equation 2.39 is the theoretical model that will be implemented for the use of TMT for CR AFM. This model is used to predict values of α , as previously discussed this non-dimensional parameter is a stiffness ratio. A ratio of stiffness of the modeled spring and stiffness of the microcantilevered beam as a quasi-static point load. This means that if the microcantilevered beam stiffness is known, then with our pre-

dicted value of α we can retrieve a stiffness value for the modeled spring. From this modeled spring, we can then retrieve the Young's modulus of elasticity. Before the model is ready for predictions it must be calibrated, which entails tuning the values of \hat{I} and Δ . The last parameter required after the calibration of the non-dimensional parameters is the contact eigenvalue for the model. This contact eigenvalue is the non-dimensional frequency which is calculated through a traditional CR AFM technique. This technique involves the use of a ratio of "free" experimental natural frequencies and in-contact experimental natural frequencies. Once these frequencies are retrieved, by using the "free" eigenvalue we can find the contact eigenvalue. This procedure will be explained in further detail in the following sections. Once the non-dimensional parameters and the contact eigenvalues are found, the model is ready for α predictions. It is important to note that, as previously discussed, continuous systems such as ours inherently possess an infinite amount of solutions or eigenvalues. Meaning, that in theory once the non-dimensional values are calibrated, we could theoretically calculate an infinite amount of contact eigenvalues to use in our model. The use of higher modes of vibration and higher contact eigenvalues leads to different predictions of α , than the predictions obtained through lower modes of vibration. This is observed and discussed in the results section.

As previously mentioned, by inputting a set of frequencies, a free-frequency and a coupled-frequency, into the theoretical model, we can predict a value of α , which can be used to obtain the Young's modulus of elasticity for a given sample. The prediction procedure is explained in further detail in the following sections, but Figure 2.4 shows the simplified procedure. Before our model can be used to reproduce accurate values we must calibrate the model by means of our non-dimensional parameters, Δ , \hat{I} and $\beta_n L$. The non-dimensional stiffness parameter, α , will help us tune the final

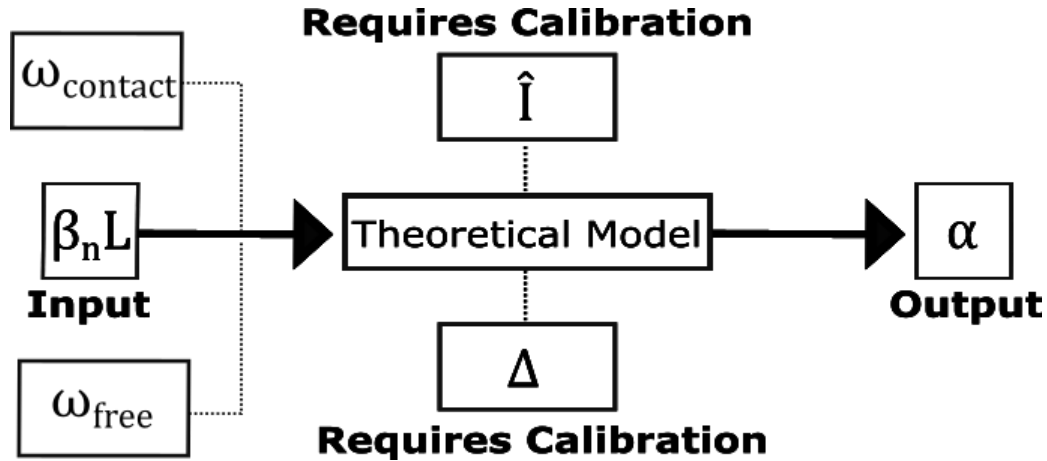


Fig. 2.4. Flow chart depicting procedure for predictions of α . By inputting a free and a contact natural frequency along with the corresponding non-dimensional solution ($\beta_n L$) into the theoretical mode, we can make predictions once our non-dimensional parameters \hat{I} and Δ are calibrated.

calibration of our model in order to verify if our property prediction for the Young's modulus of elasticity is accurate. This is done by comparing the predicted value of α from our model versus the prescribed value of α from the 3D finite element model. Since we have control over the stiffness coefficient for the spring and the cantilever's stiffness coefficient in our 3D finite element model, we can use the free and coupled frequencies retrieved from our 3D finite element model, input them into the theoretical model and compare the value of α retrieved by our model versus the value of α calculated from our 3D finite element model. In the next section, we explain the calibration procedure for each non-dimensional parameter and the techniques involved with the retrieval of α .

2.3 Calibration: Non-dimensional Parameters \hat{I}, Δ and α

As previously mentioned, the use of CR AFM as a material property retrieval technique requires the implementation of a theoretical mathematical model. This

model is designed as close as possible to the physical model's parameters. Therefore, close attention should be paid to the geometrical nature of the physical system, since the resulting Char. Eq. will be used to predict said material properties. The Char. Eq. we have derived in the previous section is particularly tailored for the Trolling Mode experimental setup. The rotational inertia effect due to the long nanoneedle has been taken into consideration, as well as the added mass effect for the needle and the mounting tip. These effects were accounted for in our derivation when we defined our boundary conditions back in Equations 2.14 and 2.15. As we mentioned in the last section, in order to use this theoretical model, the non-dimensional parameters must be calibrated. These non-dimensional parameters are what quantify the effects of the previously defined boundary conditions. In order for us to calibrate and retrieve the value of these non-dimensional parameters, we must perform a few experimental and computational procedures. We provide and discuss these techniques in order to retrieve the values for our non-dimensional parameters in the following subsections. Once these values are known, the model can be used to predict a value for α , which in turn can be used to retrieve the value of k . Then, the value of k can be used to retrieve Young's modulus of elasticity for the sample. This prediction procedure will be further explained after the non-dimensional parameter retrieval technique and calibration is described.

2.3.1 Non-dimensional Parameter \hat{I} : Torsional Trolling

Recalling from previous sections, our theoretical model is a function of a few non-dimensional parameters. Among these parameters we have the non-dimensional inertia (\hat{I}). From Equation 2.21, we recall that our non-dimensional inertia parameter \hat{I} is a ratio of the mass moment of inertia for the added nanoneedle (I_o) and the mass moment of inertia for the microcantilevered beam (ρAL^3). The mass moment of

inertia for the nanoneedle is unknown, while we make the assumption that the values for the density (ρ), cross sectional area (A) and length of the beam (L) are known.

In order to obtain the mass moment of inertia for the nanoneedle, we implement the use of a theoretical model similar to the one we have derived in previous sections. Although both models are tailored for the same TMT experimental setup, our previously derived model is based on the transverse vibrations of the microcantilevered beam AFM probe. Meanwhile, the model we will derive in this section is based on the torsional vibrations of the microcantilevered beam AFM probe. The proposed model can be observed in Figure 2.5.

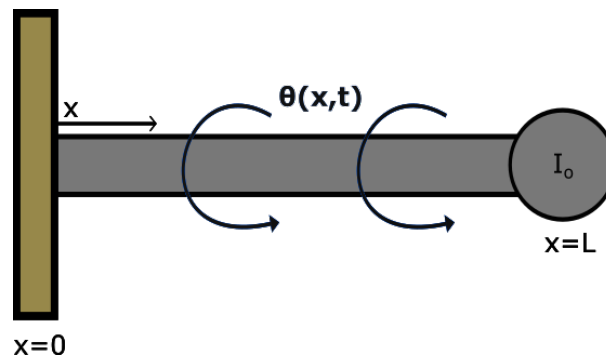


Fig. 2.5. Proposed Theoretical Model for Implementation of TMT for CR AFM, where $\theta(x, t)$ is the torsional displacement for the model and I_o is the mass moment of inertia of the nanoneedle.

We begin the derivation of this model from the equation of motion for the free torsional vibrations for a circular shaft. Although our model is not a circular shaft, we use this technique to try to derive a baseline model. Upon derivation of this model, we can add detail and increase fidelity by taking into consideration the non-circular nature of our model. This is further developed in a later section, where we show the effect of using the same derived model with a different torsional rigidity to account for the non-circular cross sectional area.

The equation of motion that describes the torsional displacements of our micro-cantilevered beam during torsional vibrations is

$$c^2 \frac{\partial^2 \theta(x, t)}{\partial x^2} = \frac{\partial^2 \theta(x, t)}{\partial t^2}, \quad (2.40)$$

where $\theta(x, t)$ is the angular displacement for our model as a function of space and time,

$$c = \sqrt{\frac{G}{\rho}}, \quad (2.41)$$

and G and ρ are the shear modulus of elasticity and the density of the microcantilevered beam, respectively. By assuming the solution as

$$\theta(x, t) = \Theta(x)T(t), \quad (2.42)$$

where $\Theta(x)$ is a function of x only and $T(t)$ is a function of t only. By substituting Equation 2.42 into Equation 2.40, we obtain

$$\frac{c^2}{\Theta(x)} \frac{d^2 \Theta(x)}{dx^2} = \frac{1}{T(t)} \frac{d^2 T(t)}{dt^2}. \quad (2.43)$$

Noting that the LHS of Equation 2.43 depends only on x and the RHS depends only on t . Their common value must be constant and in this case we denote this constant as $-\omega_t^2$. Equation 2.40 can be written as two separate equations:

$$\frac{d^2 \Theta(x)}{dx^2} + \frac{\omega_t^2}{c^2} \Theta(x) = 0, \quad (2.44)$$

$$\frac{d^2 T(t)}{dt^2} + \omega_t^2 T(t) = 0. \quad (2.45)$$

The solutions of Equations 2.44 and 2.45 can be expressed as

$$\Theta(x) = A \cos \frac{\omega_t x}{c} + B \sin \frac{\omega_t x}{c} \quad (2.46)$$

$$T(t) = C \cos \omega_t t + D \sin \omega_t t, \quad (2.47)$$

where A , B , C , and D are constants that are determined by the system's boundary conditions [27].

Now, we must enforce our previously discussed boundary conditions. First, we translate them into their mathematical equivalent. Note that for the torsional vibrations case we will only need two boundary conditions since the equation of motion is a second order partial differential equation, meanwhile for the transverse case we required four boundary conditions since the equation of motion is a fourth order partial differential equation. These two boundary conditions are still of the geometrical and natural nature. For the geometrical boundary condition we develop a relationship as a function of displacement for $\theta(x, t)$. In this case our relationship displacement for the proposed model at $x = 0$ is

$$\theta(0, t) = 0, \quad (2.48)$$

meaning that at $x = 0$, our model is constrained and therefore cannot rotate in the θ direction. Therefore, we can also say that

$$\Theta(0) = 0, \quad (2.49)$$

and now we can evaluate Equation 2.46, our spatial solution, for the fixed condition at $x = 0$, resulting in

$$A = 0. \quad (2.50)$$

This results in the reduced spatial solution of

$$\Theta(x) = B \sin \frac{\omega_t x}{c} \quad (2.51)$$

We now move on to the natural boundary condition located at the end of the microcantilevered beam. For this condition, we develop a relationship as a function of the torque experienced by the model. In this case, the torque is defined as

$$M_t = GJ \frac{\partial \theta}{\partial x} \quad (2.52)$$

Where M_t is the torque experienced by the model, G is the shear modulus of elasticity and J is the polar area moment of inertia for the microcantilevered beam. In this case, we examine the torque experienced by the model at $x = L$, where the dynamics of the nanoneedle govern this portion of the model. Therefore, we write the following relationship

$$GJ \frac{\partial \theta(L, t)}{\partial x} = -I_o \frac{\partial^2 \theta(L, t)}{\partial t^2}. \quad (2.53)$$

Where I_o is the mass moment of inertia for the nanoneedle. We now substitute our reduced spatial solution from Equation 2.51 into our newly defined natural boundary condition, obtaining

$$GJ \frac{\omega_t}{c} \cos \frac{\omega_t L}{c} = I_o \omega_t^2 \sin \frac{\omega_t L}{c}. \quad (2.54)$$

By rearranging and simplifying Equation 2.54 we obtain

$$\tan \frac{\omega_t L}{c} = \frac{GJ}{I_o c \omega_t}. \quad (2.55)$$

If we recall from our separation of variables procedure we observe in Equation 2.44, we can say that

$$\beta_t = \frac{\omega_t}{c}. \quad (2.56)$$

Where β_t is an auxiliary variable that helps us find solutions for our model. Therefore, by multiplying the RHS of Equation 2.55 by $\frac{c}{c}$, and by substituting Equation 2.56 into Equation 2.55 we obtain the following

$$\tan(\beta_t L) = \frac{GJ}{c^2 I_o \beta_t}. \quad (2.57)$$

As previously mentioned, we must maintain our model as a function of non-dimensional parameters. Therefore, we multiply the RHS by $\frac{L}{L}$ in order to keep our eigenvalue solutions in the non-dimensional terms of $\beta_t L$. After further rearranging, our equation becomes

$$\beta_t L \tan(\beta_t L) = \frac{GJL}{c^2 I_o}. \quad (2.58)$$

We further simplify by substituting Equation 2.41 into Equation 2.58.

$$\beta_t L \tan(\beta_t L) = \frac{\rho J L}{I_o}. \quad (2.59)$$

We then introduce our torsional non-dimensional inertia parameter \hat{I}_t .

$$\hat{I}_t = \frac{\rho J L}{I_o}. \quad (2.60)$$

Where \hat{I}_t is the torsional non-dimensional inertia, I_o is the mass moment of inertia for the nanoneedle, and J is the polar moment area of inertia for the microcantilevered beam.

Therefore, for torsional vibrations the theoretical model has the following characteristic equation:

$$\hat{I}_t = \beta_t L \tan(\beta_t L) \quad (2.61)$$

Now that we have our Char. Eq. for torsional vibrations of our model, we present the following technique in order to retrieve our value of interest I_o , the mass moment of inertia for the nanoneedle.

We begin by recalling from our derivation and from Equation 2.56

$$\beta_t L = \omega_t \frac{L}{C}, \quad (2.62)$$

and substituting Equation 2.62 into Equation 2.61 we obtain

$$\hat{I}_t = \omega_t \frac{L}{C} \tan(\omega_t \frac{L}{C}). \quad (2.63)$$

If we recall from our previous derivation for the transverse vibrations, we found that continuous systems inherently possess an infinite amount of solution or non-dimensional eigenvalues $\beta_t L$. And as we can observe from Equation 2.62, there is a direct relationship between our non-dimensional eigenvalue and the natural frequencies of the model. Therefore, we can further elaborate and say that the Char. Eq. for our model is

$$\hat{I}_t = \omega_{t_n} \frac{L}{C} \tan(\omega_{t_n} \frac{L}{C}). \quad (2.64)$$

Where ω_{t_n} represents the n th natural frequency of the system. We can use this to our advantage in order to find our value of I_o . If we recall Equation 2.60 we can observe that our torsional non-dimensional inertia is a ratio of

$$\frac{\rho J L}{I_o}. \quad (2.65)$$

Since the values for ρ , J and L are known, if we find the value of \hat{I}_t , we can find the value for I_o .

By means of a modal analysis on the 3D finite element model observed in Figure 2.1, we can obtain simulated experimental natural frequencies for our first and second torsional modes of vibration. These frequencies should be directly correlated to the first and second solutions obtained by our model.

From Equation 2.63, we can find the value of \hat{I}_t by plotting the Char. Eq. for ω_1 and ω_2 obtained from our modal analysis simulated data. By varying the value of $\frac{L}{C}$ and plotting our Char. Eq. for ω_1 and ω_2 simultaneously, we find a solution for the value of \hat{I}_t . This occurs at the location where both functions cross, leading to the same value of \hat{I}_t for both ω_1 and ω_2 . The simulated torsional frequencies obtained were $4.560 \frac{rad}{\mu s}$ and $5.842 \frac{rad}{\mu s}$. Through our graphical approach, we can observe that the solution where both equations cross is located at 4.556 for \hat{I}_t . From Equation 2.60, we recall that we assumed that the density (ρ), length (L) and polar moment area of inertia (J) for the beam were known and we found the value for our non-dimensional torsional inertia. Therefore, we can now find a value for the mass moment of inertia for the nanoneedle. Here we assume symmetric proportions for the cross sectional area in order to translate the mass moment of inertia in the torsional directions versus the transverse direction. In our 3D model the nanoneedle's cross sectional area is a rectangle. This was due to 3D model complications. Therefore, this is also a parameter that could be updated for higher fidelity models. Once we find the mass

moment of inertia for the nanoneedle, I_o , we can substitute it into Equation 2.21 in order to obtain our first non-dimensional parameter, \hat{I} , for our transverse theoretical model. Therefore, I_o becomes the product of our non-dimensional torsional inertia, \hat{I}_t and ρJL . In this case, for the product of ρJL , we are assuming the density and length of the microcantilevered beam to be $2320 \frac{kg}{m^3}$ and 200×10^{-6} m, respectively. For the value of the polar moment area of inertia, J , we calculate as follows

$$J = \frac{bt}{12}(b^2 + t^2). \quad (2.66)$$

Where b and t are our width and thickness, respectively. Finding our value of J to be $4.52 \times 10^{-21} m^4$, thus the product of ρJL is 2.09728×10^{-22} . Now we can find our value for I_o ,

$$I_o = \frac{\rho JL}{\hat{I}_t} = \frac{2.09728 \times 10^{-22}}{4.556} = 4.60 \times 10^{-22}. \quad (2.67)$$

Now that we have retrieved the mass moment of inertia for the nanoneedle, I_o , we can go back to our transverse theoretical model in Equation 2.39 and refer to Equation 2.21, where we assume the values for ρ, A, L are known and we now have the value for I_o , the mass moment of inertia for the nanoneedle. We can now calculate the first non-dimensional parameter, \hat{I} , for our transverse theoretical model,

$$\hat{I} = \frac{I_o}{\rho AL^3} = \frac{4.60 \times 10^{-22}}{1.1136 \times 10^{-18}} = 4.1307 \times 10^{-4}. \quad (2.68)$$

We have successfully found the non-dimensional inertia parameter for our model and move on to finding the non-dimensional mass parameter, Δ .

2.3.2 Non-dimensional Parameter Δ : Free Vibrations

Recalling Equation 2.25, our non-dimensional mass parameter, Δ , is a ratio of masses between the nanoneedle and the microcantilevered beam. In order to solve and calibrate this non-dimensional parameter, we use the “free” version of our proposed model for transverse vibrations in Equation 2.39. By free, meaning the microcantilevered AFM probe is not in contact with the sample. This translates to a no-spring setting for our model, or simply setting the value of α to zero, as can be seen in Figure 2.6. The resulting model can then be expressed as

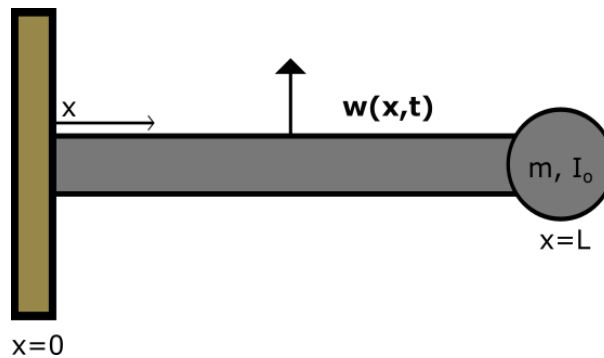


Fig. 2.6. Proposed Theoretical Model for Implementation of TMT for CR AFM where $w(x, t)$ represents the transverse displacement over time of the model, m is the added mass of the nanoneedle and I_o is the mass moment of inertia of the nanoneedle.

$$f(\beta L, \hat{I}, \Delta, 0) = 0, \quad (2.69)$$

where the value of \hat{I} is now known and the value of Δ is what we are interested in finding. From previous sections, we discussed that a continuous system, such as ours, possesses an infinite amount of solutions. In this case, we mentioned these solutions were the non-dimensional eigenvalues $\beta_n L$. Where the sub-index n denotes to which eigenmode the eigenvalue corresponds to. Meaning, that if in our case an

eigenvalue corresponds to a natural frequency, then our eigenmode corresponds to a mode of vibration. For our case, this means that every mode of vibration reproduces a different shape, called eigenshapes, of our microcantilevered beam. Therefore, the first solution found for our model would correspond to the first eigenvalue, which translates to the first natural frequency for our model. This first natural frequency dictates the shape our microcantilevered beam will take for the first mode of vibration. Following the same logic, the second solution found for our model would be the second eigenvalue, which translates to the second natural frequency for our model. This new natural frequency now dictates the new shape the microcantilevered beam will take in the second mode of vibration. Therefore, every solution is associated with its own particular shape for that particular mode. We can use these properties to our advantage to create a ratio of eigenvalues between one mode and the following mode. The use of this eigenratio will then allow us to retrieve a value for Δ , as we show in the following technique.

First, we rearrange the relationship between our natural frequency and our eigenvalue for transverse vibrations in Equation 2.18 as

$$\omega_n = (\beta_n L)^2 \sqrt{\frac{EI}{\rho AL^4}}. \quad (2.70)$$

Therefore, if we were to create a natural frequency ratio between the natural frequency at a latter mode and a natural frequency at the current mode we would obtain

$$\frac{\beta_{n+1} L}{\beta_n L} = \sqrt{\frac{\omega_{n+1}}{\omega_n}}. \quad (2.71)$$

Where the index n , represents the current mode of vibration or eigenmode, and thus creating the relationship for our eigenratio. We will use this eigenratio to find our value of Δ as previously mentioned. We do this by obtaining the first two free

transverse natural frequencies from our 3D finite model through means of a transverse modal analysis. Notice that similarly to the no-spring setting for our theoretical model, our 3D finite model also lacks a springs, therefore outputting free natural frequencies. The simulated natural frequencies for the first and second transverse mode of vibration are $3.7443 \times 10^{-1} \frac{rad}{\mu s}$ and $2.4372 \frac{rad}{\mu s}$. By dividing these two natural frequencies, we then obtain a value for our eigenratio

$$\frac{\beta_{j+1}L}{\beta_jL} = \sqrt{\frac{\omega_{j+1}}{\omega_j}} = 2.5514. \quad (2.72)$$

Now that we found the value of our eigenratio, we can use our theoretical model with our no-spring setting in order to find the value of Δ with the following method. For

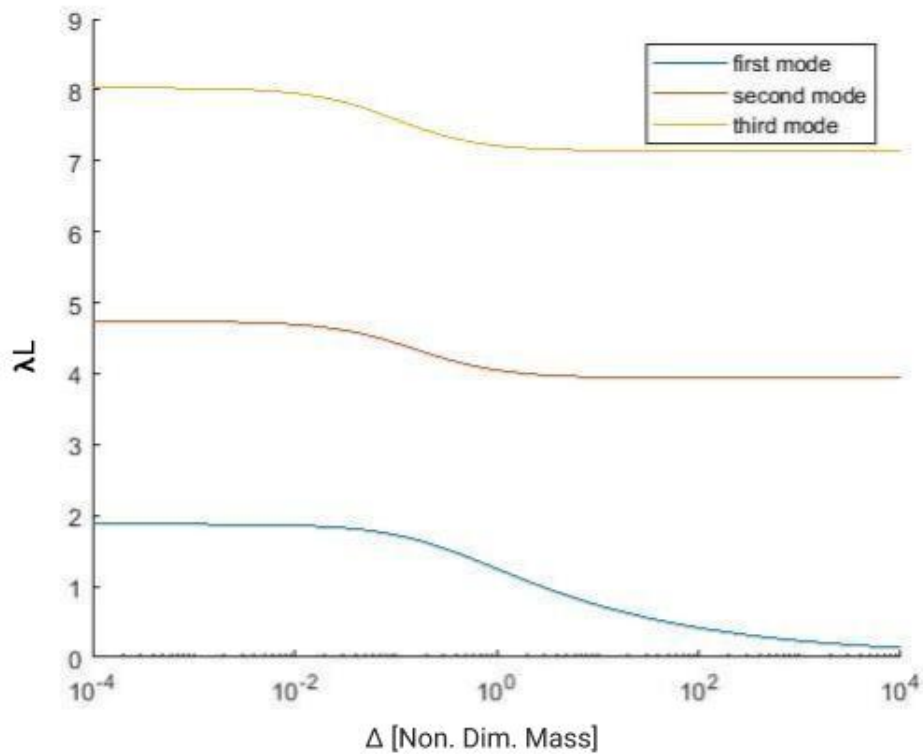


Fig. 2.7. Theoretical Eigensolutions Array Versus delta Array

our no-spring theoretical model in Equation 2.69, we can assign an array of values to Δ . This array of solutions is created taking into consideration what Δ represents. Since Δ is the mass ratio for the nanoneedle and the beam, there are only so many values for Δ , considering the typical size of the nanoneedle. Having taken this into consideration, we create array for Δ , which ranges for values of 10^{-4} to 10^4 in the log-scale. Therefore, we are left with one unknown, the eigenvalue. In order to find this eigenvalue, we use a “root” solving computational technique that finds the first three eigenvalues to our no-spring Char. Eq. for every different value of Δ , which then creates three arrays of eigensolutions for varying values of Δ . These arrays can be seen on the graph in Figure 2.7.

Once we have found these arrays, we can divide the array of eigensolutions for the second mode of vibration by the array of eigensolutions for the first mode of vibration. The division of these two arrays then results in a graph that can be observed in Figure 2.8. Earlier, we found the value of our eigenratio for the 3D finite element model to be 2.5514. Therefore, by inspection, we can find in the theoretical eigenratio graph from Figure 2.8 for what value of Δ does the theoretical eigenratio equal our simulated eigenratio, 2.5514.

As we can observe in Figure 2.8, our corresponding value for Δ is 0.0714. Therefore, we have found our non-dimensional mass parameter for our proposed transverse theoretical model.

For the two past sections we have been calibrating and solving for non-dimensional parameters based on our TMT experimental setup. Through the use of our simulated data and theoretical solutions, we now have the necessary parameters to use our proposed model. We continue with the standard contact resonance technique for solutions of α , the non-dimensional stiffness ratio, by the use of the in-contact and free frequency technique.

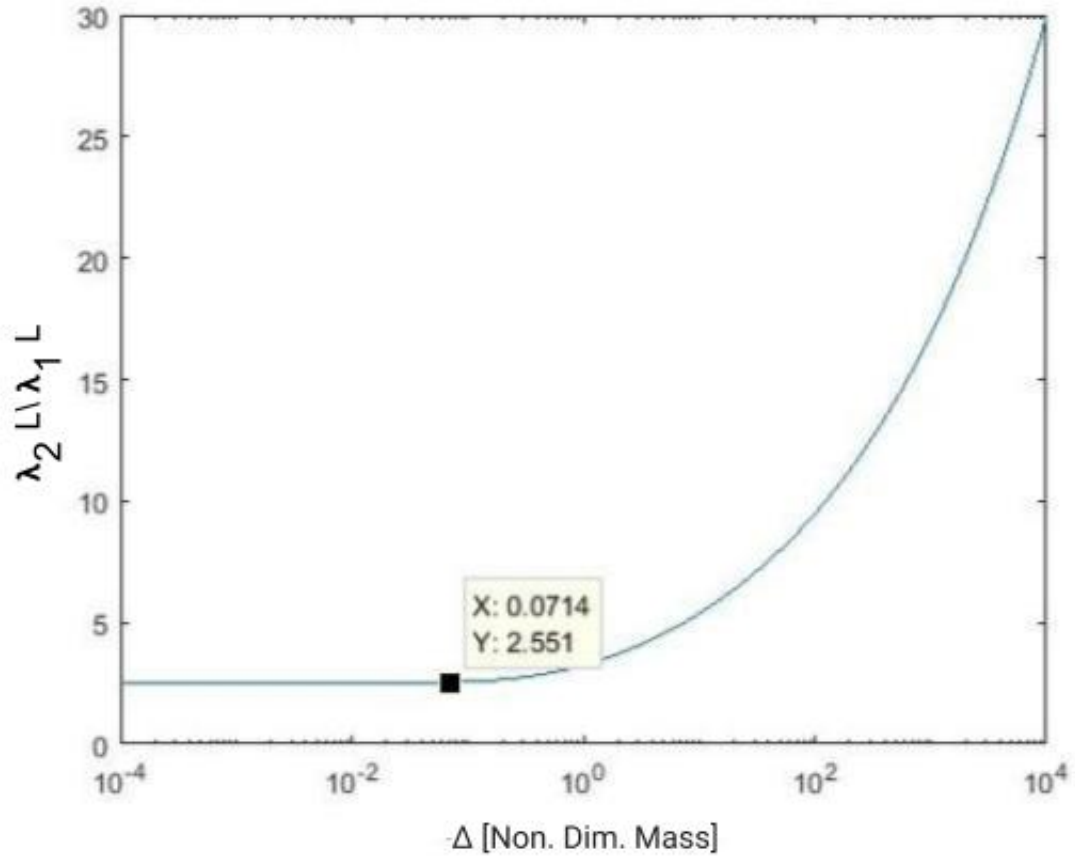


Fig. 2.8. Theoretical Eigenratio Array Versus delta Array

2.3.3 Non-dimensional Parameter $\beta_n L$: Frequency Ratios to Predict α

Recalling our proposed model in Equation 2.39,

$$f(\beta_n L, \hat{I}, \Delta, \alpha) = 0,$$

we now have values for the inertia non-dimensional parameter (\hat{I}) and the mass non-dimensional parameter (Δ), as well. Therefore, we only need a value for $\beta_n L$ and our

model is almost ready to be used for elasticity predictions. In this case, the value to predict is α . Recalling equation 2.27

$$\alpha = \frac{k}{k_c},$$

we can observe that if k_c is known, by finding α , we can predict values for k , the spring stiffness in our model. From the spring stiffness predicted, we can extrapolate the Young's modulus of elasticity for the sample. In this case, the value for k is known and can be controlled in our 3D finite element. However, in our theoretical model, the value for k is unknown. Therefore, we must predict a value of α in order to obtain a value for k in our theoretical model. If our value of α predicts the value of k selected in our 3D finite element model, then we have successfully calibrated our theoretical model.

In order to complete this calibration, the only value we need to find in order to start making predictions for values of α is our eigenvalue $\beta_n L$. In this case, the eigenvalue would correspond to the contact non-dimensional frequency, rather than the free non-dimensional frequency, since our model is no longer on the no-spring setting. Therefore, since our value for α is not zero, this means we are in-contact. Unfortunately, the 3D finite element model can only retrieve dimensional natural frequencies and the mathematical model needs non-dimensional natural frequencies in order to make predictions for values of α . Therefore the contact eigenvalue, $\beta_{\text{contact}} L$, cannot be retrieved through means of our 3D finite element model. Instead, we use a common CR AFM technique involving free and in-contact frequency ratios. Once we find this contact eigenvalue we can use it along with our calibrated values in order to being making predictions for values of α . Since there are an infinite amount of contact eigenvalues we can find, this means that we can use our model for any given mode of

vibration to make predictions. The only requirement is that we use the corresponding eigenvalue for the mode of vibration we are examining at the time.

We create a free-to-contact ratio, similarly to the way we created an eigenratio in the previous section. Instead of using a ratio of frequencies for consecutive modes of vibration, we use a ratio which involves the in-contact and free frequencies for the same mode of vibration. By doing so, we obtain the following

$$\frac{\omega_{\text{contact}}}{\omega_{\text{free}}} = \frac{(\beta_{\text{contact}}L)^2}{(\beta_{\text{free}}L)^2}. \quad (2.73)$$

Rearranging Equation 2.73 we obtain

$$\beta_{\text{contact}}L = \beta_{\text{free}}L\sqrt{\frac{\omega_{\text{contact}}}{\omega_{\text{free}}}}. \quad (2.74)$$

In this case ω_{contact} and ω_{free} are retrieved directly from our 3D contact finite element model and the “free”, or no-spring setting, 3D finite element model, where the contact frequency is based on the stiffness coefficient used in the 3D finite element model. We pick a value to calibrate the model with and then use the calibrated model to make multiple predictions for multiple springs and observe how our model matches up to the results. First, we obtain our eigenvalue $\beta_{\text{free}}L$ by using our theoretical model for the “free” case ($\alpha = 0$), as seen in Figure 2.6. Meaning by inputting our obtained values of \hat{I} and Δ into our theoretical model with the no-spring setting, we can use a root solving routine in order to find the first three eigenvalues for our model. In this case, these eigenvalues will be the free non-dimensional natural frequencies $\beta_{\text{free}}L$.

Now that we have the required frequencies and eigenvalue, we can find our $\beta_{\text{contact}}L$ for the first mode of vibration and input it into our theoretical model in order to make predictions of values for α . We calculate the contact eigenvalue as follows,

Table 2.1.

Summary of results for calculated free eigenvalues through means of the no-spring, free version of our proposed model and results for the contact and free frequencies retrieved from the 3D finite element model.

Eigenmode	Free Eigenvalue $\beta_{\text{free}}L$	Free Frequency $\omega_{\text{free}} \frac{\text{rad}}{\mu\text{s}}$	Contact Frequency $\omega_{\text{contact}} \frac{\text{rad}}{\mu\text{s}}$
1	1.7614	3.74438×10^{-1}	1.74438
2	4.4927	2.43724	3.40693
3	7.600	6.85237	6.98337

$$\beta_{\text{contact}}L = \beta_{\text{free}}L \sqrt{\frac{\omega_{\text{contact}}}{\omega_{\text{free}}}} = 3.8018. \quad (2.75)$$

We have retrieved all the necessary parameters required in order to find α using our proposed theoretical model, calibrated based on data from the first mode of vibration.

$$f^1(\beta_{\text{contact}}L, \hat{I}, \Delta, \alpha) = 0. \quad (2.76)$$

Our calibration results for the proposed model can be seen in Table 2.2.

Table 2.2.

Summary of results for calibration procedure.

Eigenmode	Eigenvalue $\beta_{\text{contact}}L$	Inertia \hat{I}	Mass Δ
1	3.8018	4.1307×10^{-4}	0.0714

When we input the values observed in Table 2.2 into our theoretical model from Equation 2.76, we retrieve a value for α which we use to retrieve a value for k . These values can then be compared to the prescribed values of α_a and k_a in our 3D finite element model to assess the calibration result.

Table 2.3.
Summary of results for first mode prediction procedure.

Predicted	Predicted	Actual	Actual
α	k	α_a	k_a
78.0570	98.9372	47.15	59.76

As we can observe in Table 2.3 , our model provides a positive prediction for α . Meaning, that the α predicted was not a negative value. Although our prediction for one value of α is not very accurate for this particular point, the positive prediction for a value of α means the model did not fail. These mathematical models are limited since they are a simplification of the real-time dynamic system. Therefore these models can predict negative values, these negative values are non-physical. From Equation 2.27, our non-dimensional stiffness ratio α is a ratio of stiffness between the spring and the microcantilever. Therefore, if the value of α predicted is negative, this would mean the spring value for stiffness would be negative, which would result in an unstable physical system. In order to accurately assess the performance of the proposed model we must test it to predict a range of values for α rather than just one value for α , as well as for different modes of vibration. Therefore in the results chapter, we assess the performance of the predictions for our proposed model for a range of values for α for the first three modes of transverse vibrations. We compare the predictions and percentage error of the baseline model and our proposed model.

Before we present the results, in the following section we present an update to the model proposed. The baseline model in Figure 1.7 shows the current mathematical model used for α predictions in CR AFM. Figure 2.3 shows the proposed mathematical model for α predictions, where the non-dimensional inertial parameter \hat{I} was found through the torsional vibrations of our model. This torsional vibration analysis was done approximating our model as a rod, this results in a simplified derivation of

the Char. Eq. for the torsional mode of vibration. We now present an update to our proposed model for the use of non-circular cross sectional areas. We do this by updating the value for our torsional rigidity. This procedure results in a more complete response for the behavior of our model, since the model now accounts for the inertial and added mass effects of the nanoneedle along with the non-circular cross sectional area.

2.4 Updating the Theoretical Model for Non-circular Cross Sections

2.4.1 Updating \hat{I}_t and \hat{I} for Non-circular Cross Sections

The implementation of this update begins with the modification of variables defined earlier in the torsional modal analysis in Equation 2.40

$$C \frac{\partial^2 \theta(x, t)}{\partial x^2} = \rho J \frac{\partial^2 \theta(x, t)}{\partial t^2}. \quad (2.77)$$

Where ρ and J are still the density and polar area moment of inertia for the microcantilevered beam, and C is now the torsional rigidity for our microcantilevered beam. With this newly introduced parameter, we can now account for non-circular cross sectional area. The equation for the torsional rigidity is

$$C = kGt^3b \quad (2.78)$$

Where b and t are the width and thickness for the microcantilever, accordingly, and k is [27]

$$k = \frac{1}{3} \left(1 - \frac{192t}{\pi^5 b} \sum_{j=1}^{\infty} \frac{1}{(2j-1)^5} \tanh\left((2j-1)\pi \frac{b}{t}\right) \right) \quad (2.79)$$

and G is

$$G = \frac{E}{2(1 + \nu)}. \quad (2.80)$$

Where G is the shear modulus of elasticity, E is the Young's modulus of elasticity and ν is Poisson's ratio for the microcantilevered beam.

From Equation 2.77 we can re-arrange to

$$\frac{C}{\rho J} \frac{\partial^2 \theta(x, t)}{\partial x^2} - \frac{\partial^2 \theta(x, t)}{\partial t^2} = 0, \quad (2.81)$$

and define

$$\bar{c}^2 = \frac{C}{\rho J}. \quad (2.82)$$

Thus, re-defining our equation of motion from Equation 2.40 into

$$\bar{c}^2 \frac{\partial^2 \theta(x, t)}{\partial x^2} = \frac{\partial^2 \theta(x, t)}{\partial t^2}, \quad (2.83)$$

where \bar{c} is

$$\bar{c} = \sqrt{\frac{C}{\rho J}}. \quad (2.84)$$

From here the derivation up to the Char. Eq. is the same as previously derived from Equation 2.42 up to Equation 2.61. Where the final version of our new Char. Eq. is still

$$\hat{I}_t = \beta L \tan(\beta L), \quad (2.85)$$

but our value non-dimensional eigenvalue is

$$\beta L = \omega \frac{L}{\bar{c}}. \quad (2.86)$$

For the calculation of k , the infinite series in Equation 2.79 converges to the value of 0.3193. Since both the Young's modulus of elasticity and Poisson's ratio are known.

Now we can calculate the shear modulus of elasticity, G , from Equation 2.80. Now we can find our torsional rigidity, C , from Equation 2.78. Where now in our Char. Eq. we have

$$\hat{I}_t = \omega \frac{L}{\bar{c}} \tan\left(\omega \frac{L}{\bar{c}}\right), \quad (2.87)$$

where our natural frequency ω is still retrieved through means of our 3D finite element model, the value for \bar{c} can now be calculated since we know the value for our torsional rigidity, C . In this case, since we have calculated the value of \bar{c} , there is no need for a graphical approach. Since we only have a single unknown, we substitute the retrieved values into our Char. Eq. to obtain the value for \hat{I}_t . In this case the retrieved value for \hat{I}_t was

$$\hat{I}_t = 4.6290 \quad (2.88)$$

If we compare this value with the result from Section 2.1.1, 4.556, we can observe there is an adjustment that occurs for the non-dimensional torsional inertia. Recalling from Equation 2.60, our ratio for the value of \hat{I}_t is

$$\frac{\rho J L}{I_o}. \quad (2.89)$$

The density (ρ), polar area moment of inertia (J), and length (L) for the microcantilevered beam are known, therefore the mass moment of inertia for the nanoneedle is

$$I_o = \frac{\rho J L}{\hat{I}_t} = \frac{2.09728 \times 10^{-22}}{4.6290} = 4.53 \times 10^{-22}. \quad (2.90)$$

Now that we have retrieved the mass moment of inertia for the nanoneedle, we can substitute this value into Equation 2.21 in order to obtain our updated value for \hat{I} .

$$\hat{I} = \frac{I_o}{\rho AL^3} = \frac{4.53 \times 10^{-22}}{1.1136 \times 10^{-18}} = 4.0685 \times 10^{-4}. \quad (2.91)$$

We have successfully updated the non-dimensional inertia parameter for non-circular cross sectional areas. We now proceed to update the non-dimensional mass parameter, Δ .

2.4.2 Updating Δ for Non-circular Cross Section

In this procedure, we do not need to modify any parameters from the previous model used for the calibration of Δ , meaning we use the same eigenratio technique for the solution of Δ . The only difference is we now have a different value of \hat{I} that we are using to find Δ . Therefore, in 2.9, we show the last graph where we are looking for a value of Δ , which gives us the value of our eigenratio. Recalling from last section, the value we are looking for is 2.5514. In 2.9, we can observe a subtle change for our new value of Δ . Now that we have updated our inertial and mass non-dimensional parameters, we can input these into the no-spring version of our proposed model in order to obtain the “free” eigenvalues as done in the previous calibration.

2.4.3 Updating βL and New Predictions of α

With the “free” and in-contact frequencies from the 3D finite element model we can calculate our in-contact eigenvalue in order to make predictions of α . The results are as outlined in Table 2.4.

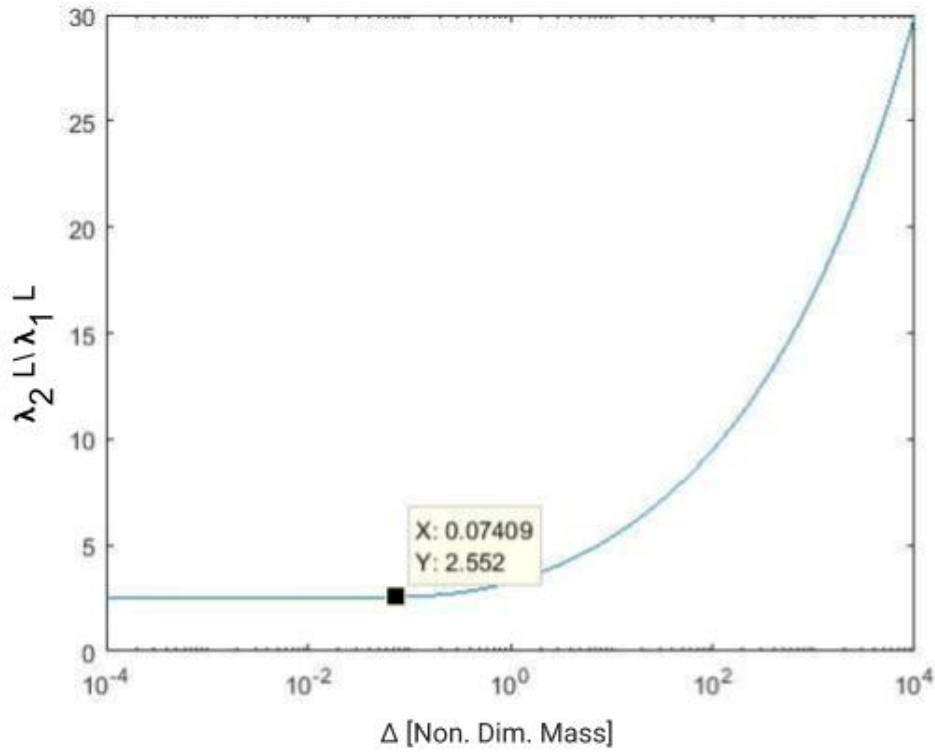


Fig. 2.9. Theoretical Eigenratio Array Versus delta Array update for non-circular cross section.

Table 2.4.

Summary of results for calculated free eigenvalues through means of the no-spring, free updated version of our proposed model for non-circular cross sectional areas and results for the contact and free frequencies retrieved from the 3D finite element model.

Eigenmode	Free Eigenvalue	Free Frequency	Contact Frequency
	$\beta_{\text{free}}L$	$\omega_{\text{free}} \frac{\text{rad}}{\mu\text{s}}$	$\omega_{\text{contact}} \frac{\text{rad}}{\mu\text{s}}$
1	1.7577	3.74438×10^{-1}	1.74438
2	4.4858	2.43724	3.40693
3	7.6497	6.85237	6.98337

Now that we have the required frequencies and eigenvalue, we can find our $\beta_{\text{contact}}L$ for the first mode of vibration for non-circular cross sectional areas and input it into our theoretical model in order to make predictions of values for α .

$$\beta_{\text{contact}}L = \beta_{\text{free}}L \sqrt{\frac{\omega_{\text{contact}}}{\omega_{\text{free}}}} = 3.7938, \quad (2.92)$$

We have retrieved all the necessary parameters required in order to find α using our proposed theoretical model calibrated based on data from the first mode of vibration.

$$f_{\text{updated}}^1(\beta_{\text{contact}}L, \hat{I}, \Delta, \alpha) = 0. \quad (2.93)$$

Table 2.5.

Summary of results for updating procedure for non-circular cross sectional areas.

Eigenmode	Eigenvalue	Inertia	Mass
	$\beta_{\text{contact}}L$	\hat{I}	Δ
1	3.7938	4.0685×10^{-4}	0.07409

Table 2.6.

Summary of results for first mode non-circular cross sectional areas prediction procedure.

Predicted	Predicted	Actual	Actual
α	k	α_a	k_a
74.2323	94.0869	47.15	59.76

As shown in 2.5 and 2.6, we can observe slight improvement in predictions, although we are still off by a significant amount and this is still only for a single value of α . In order to assess the performance of our updated model we test our predictions versus a range of values for α . In the following chapter we observe, compare and discuss the performance of the baseline model, our proposed model and the updated version of our proposed model for non-circular cross sectional areas.

3. RESULTS

In the following section, we will compare and discuss the results for the baseline model, our proposed model and the updated model for a non-circular cross sectional area. We assess the performance of these three models based on their predictions for α using the first three modes of transverse vibration.

These different sets of predictions for α are compared versus the prescribed values of α used in the 3D finite element model simulation. The prescribed values for α are calculated through Equation 2.27 by using the range of values for the stiffness of the springs used in the simulation, and the calculated cantilever stiffness from the material properties used for the 3D finite element model.

3.1 Baseline Model: Predictions for α

3.1.1 Using the First Mode of Transverse Vibration

First we present the predictions of α for the baseline model based on the first mode of transverse vibration, which can be observed in Figure 1.7. The graph in Figure 3.1 shows a red line which represents the prescribed values of α from the different modal simulations performed for our 3D model.

These values of α were defined as 50 equally logarithmically spaced points from 10^{-2} to 10^{10} . Meaning, that our actual α array consists of 50 different values for α equally spaced from 10^{-2} to 10^{10} . If we recall from Equation 2.27, our value of α is a ratio of the coefficient of stiffness for the spring and the coefficient of stiffness for the microcantilevered beam. Therefore, the increase in α results in an increase of

stiffness for the spring, and a decrease in α results in a decrease of stiffness for the spring.

As we can observe from Figure 3.1, the baseline model appears to have accurate predictions, but begins to fail as we approach 10^2 in the x-axis. The reason why the model fails as we increase values of α is due to the limited sensitivity the AFM has after a particular stiffness ratio. Meaning, after we reach a particular stiffness we can no longer distinguish between any further increase in stiffness. This is due to the stiffness difference between the AFM probe and the sample. The percent error graph

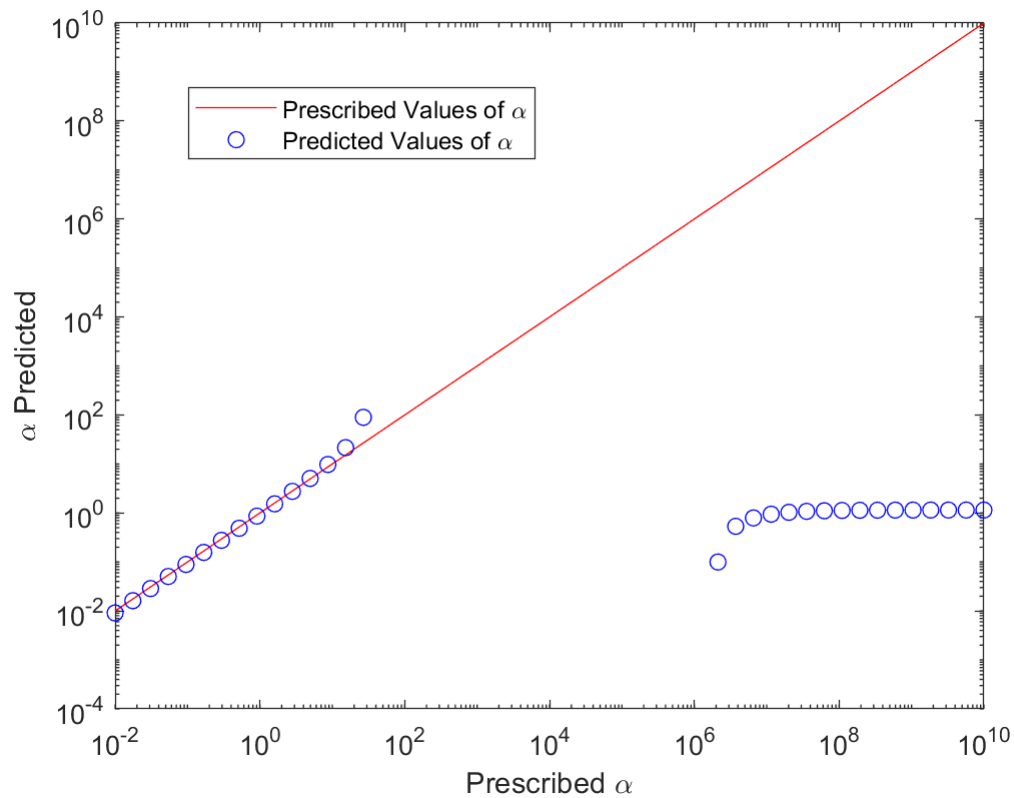


Fig. 3.1. Prescribed values for α array [Red Line] versus predicted value for α array [Blue Dots] for the baseline model for the first mode of transverse vibration, where the blue dots not seen on the plot are ignored negative values.

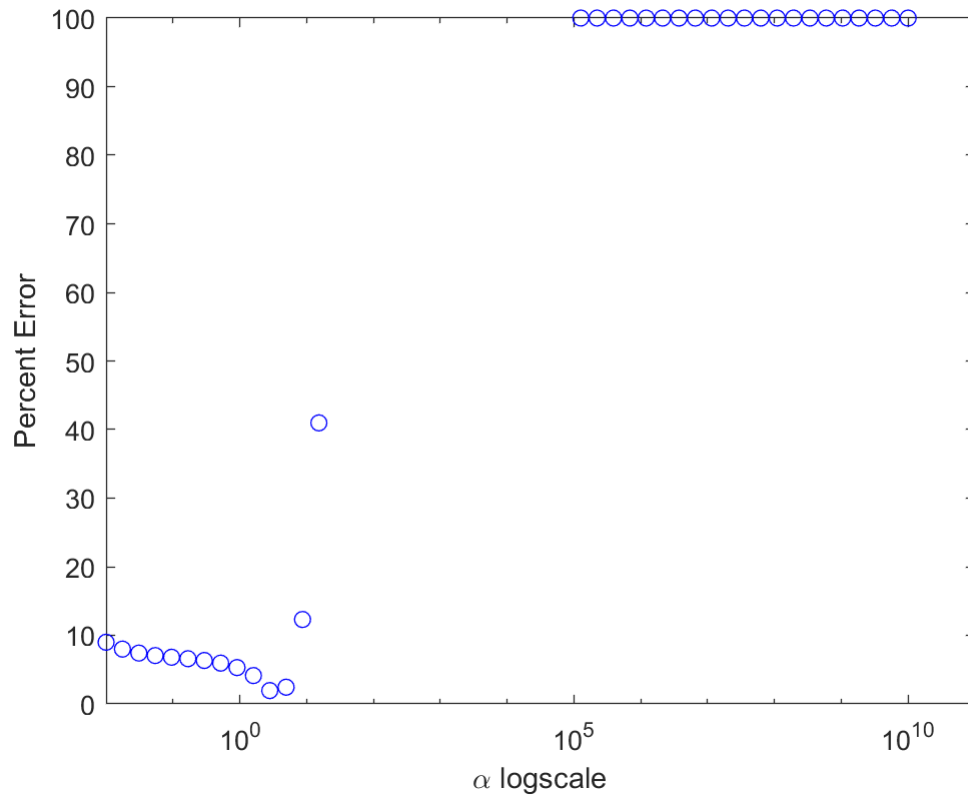


Fig. 3.2. Percent error for the individual predicted values of α for the baseline model for the first mode of transverse vibration, where the cluster of points aligned at 100 percent error are simply a product of a very small predicted value for α compared to a very large prescribed value for α .

for each individual case can be seen in Figure 3.2. This graph reveals that the effective range for α prediction using the baseline model is from 10^{-2} to 10^1 . In this range, the baseline theoretical model gives predictions within a 10 percent margin error. It is important to notice the behavior of the model once we reach values of 10^5 . This cluster of data points exactly at 100 percent is a result of a much smaller predicted value for α and a much larger prescribed value for α . This behavior is observed in all models, as we will see in the following sections, therefore when doing a comparison

of percent error for the three models, we will not include the cluster of values at 100 percent.

3.1.2 Using the Second Mode of Transverse Vibration

Using the second mode's data, meaning using the free eigenvalue, free natural frequency and contact natural frequency for the second mode of transverse vibration, we obtain the following predictions for values of α .

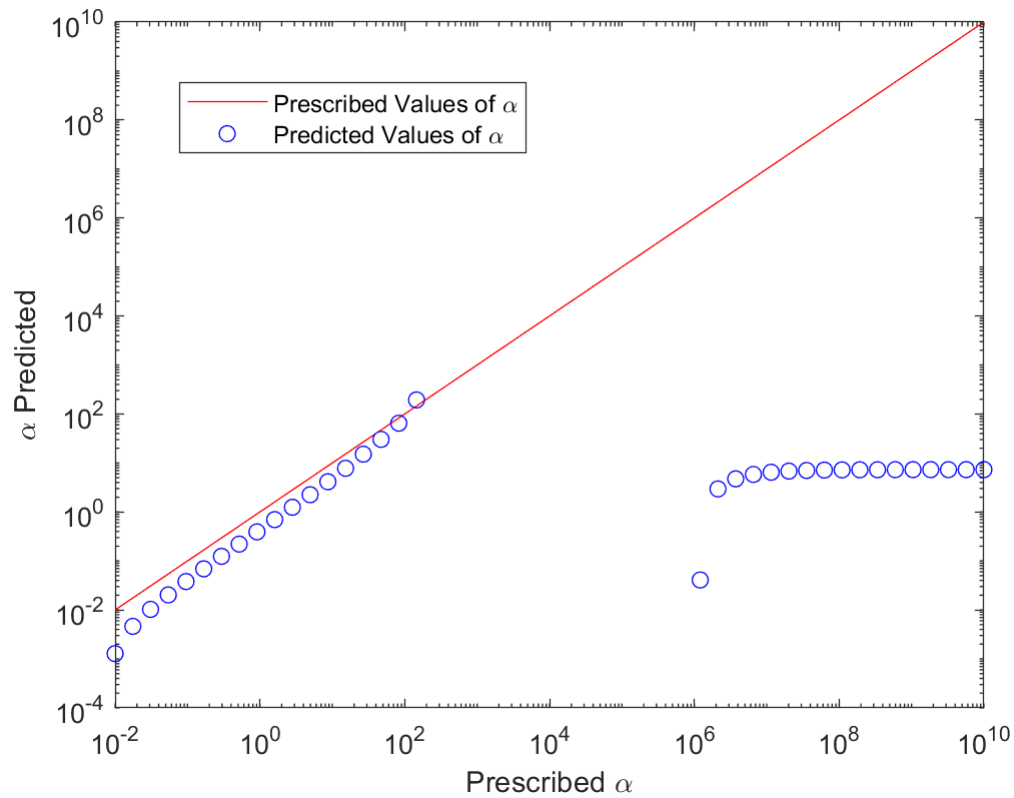


Fig. 3.3. Prescribed values for α array [Red Line] versus predicted value for α array [Blue Dots] for the baseline model for the second mode of transverse vibration, where the blue dots not seen on the plot are ignored negative values.

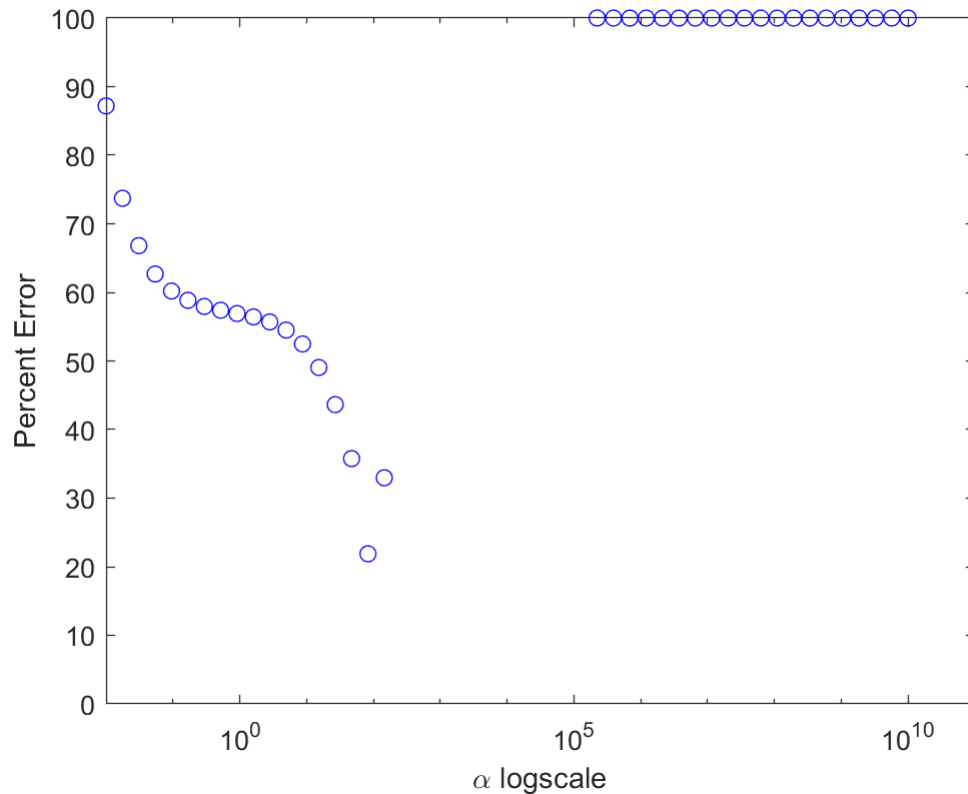


Fig. 3.4. Percent error for the individual predicted values of α for the baseline model for the second mode of transverse vibration, where the cluster of points aligned at 100 percent error are simply a product of a very small predicted value for α compared to a very large prescribed value for α .

It becomes evident from the predictions in Figure 3.3 that the model quickly veers away from the prescribed values of α . From the percent error graph in Figure 3.4, we can see the model no longer has reliable predictions for the effective range observed from the first mode. The percent error is almost 100 percent for the first α prediction. An interesting thing to notice is that the baseline model provided accurate predictions within 10 percent for the first mode of vibration, meanwhile the model failed to even provide a prediction within 10 percent for the second mode. The dramatic change in accuracy is due to the relationship between the stiffness and the higher modes of

vibration. This means that through higher modes of vibration we are able to expand the effective range for which we could make predictions for α . The lower modes of vibration are optimal for lower values of α or softer samples, meanwhile the higher modes of vibration are optimal for stiffer samples. The second mode of vibration is still considered a lower mode, so the failure of the model is not due to the previously mentioned relationship. A possible reason for the drastic change in accuracy from the first mode to the second mode is due to the dynamics of the nanoneedle. Meaning, that the natural frequency for the first mode of vibration is not sufficient to excite the dynamics of the nanoneedle. Therefore, the model behaves closer to the baseline model since the nanoneedle dynamics are not contributing significantly. When we use the data from the second mode of vibration, the natural frequency is much higher, thus resulting in a higher involvement of the nanoneedle dynamics. Now, a more representative behavior of the model's dynamics is activated through the natural frequencies for the second mode of transverse vibration.

3.2 Proposed Model: Predictions for α

3.2.1 Using the First Mode of Transverse Vibration

We now present the predictions for values of α for the proposed model seen in Figure 2.3. This model does not consider the non-circular cross sectional area, but incorporates the inertial effect and added mass effect of the nanoneedle. The graph in Figure 3.5 shows our model's performance for the first mode of vibration versus the prescribed values of α , represented by the red line. The proposed model has similar predictions as the baseline model, but here it appears that our proposed model veers off later than the baseline model, therefore increasing the effective range for predictions of α . The percent error for each individual predicted α can be seen in

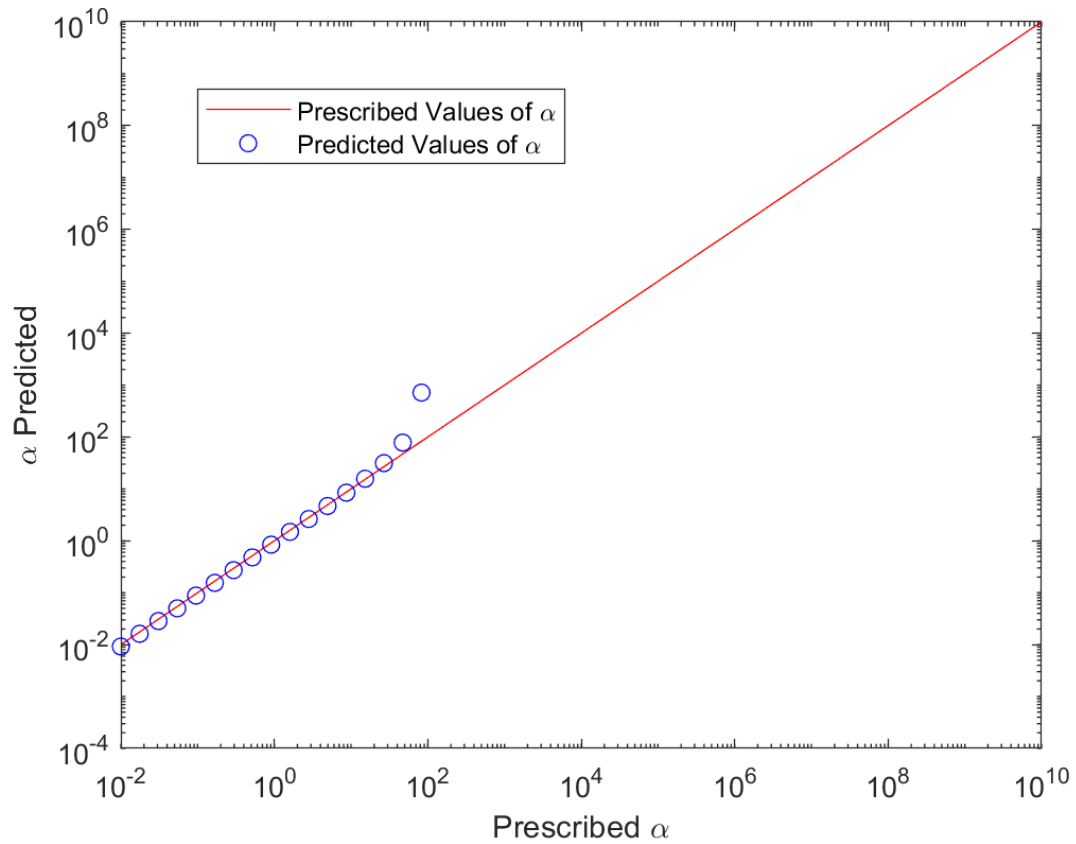


Fig. 3.5. Prescribed values for α array [Red Line] versus predicted value for α array [Blue Dots] for the proposed model for the first mode of transverse vibration, where the blue dots not seen on the plot are ignored negative values.

Figure 3.6. This percent error graph shows accurate predictions within 10 percent of the prescribed value of α . Similarly to the baseline model, it begins to diverge around a value of 10^2 for α . In order to better assess the performance of the proposed model, it is imperative we use the data from the second mode of vibration. As seen in the previous section, the baseline model failed to predict values for α accurately for the second mode. Therefore, we present the results for the second mode of vibration.

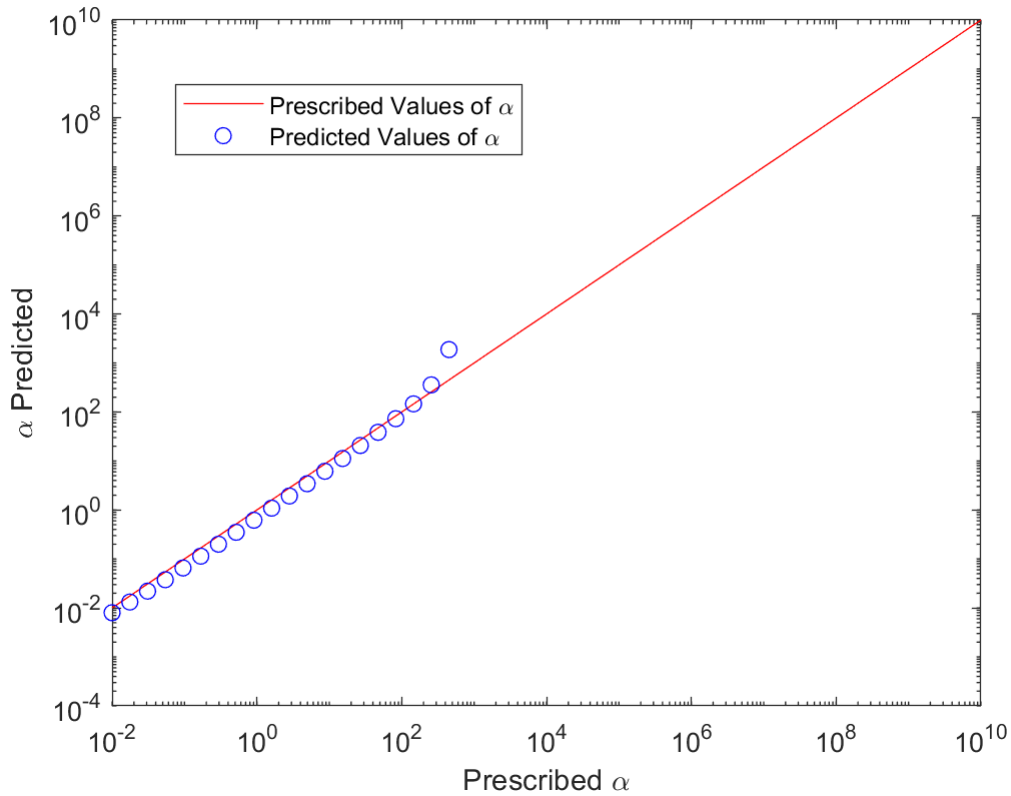


Fig. 3.7. Prescribed values for α array [Red Line] versus predicted value for α array [Blue Dots] for the proposed model for the second mode of transverse vibration, where the blue dots not seen on the plot are ignored negative values.

model. The proposed model predicts within 30 percent of the prescribed value of α for the second mode. Recalling from Figure 3.2, we can observe almost 100 percent error for the first prediction, slowly decreasing in percent error with every value of α . However, the best prediction given by the baseline model for the second mode of vibration was only within 20 percent of the prescribed value for α . Meanwhile, our first prediction for the value of α using the proposed model was already within 20 percent. The percent error, as can be seen in Figure 3.8, is contained within the 30 percent for an effective range of 10^{-2} to 10^3 and provides almost 100 percent accuracy for the range of 10^3 for values of α .

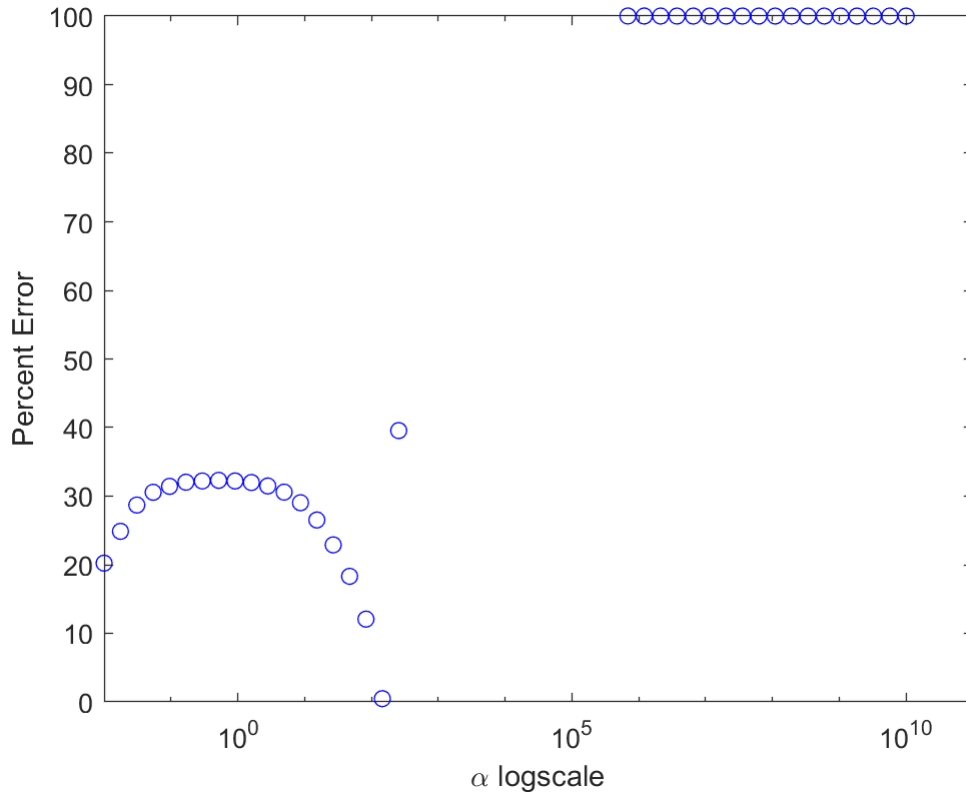


Fig. 3.8. Percent error for the individual predicted values of α for the proposed model for the second mode of transverse vibrations, where the cluster of points aligned at 100 percent error are simply a product of a very small predicted value for α compared to a very large prescribed value for α

3.3 Updated Non-circular Cross Sectional Area Model: α Predictions

3.3.1 Using the First Mode of Transverse Vibration

Lastly, we present the predictions of α for the updated non-circular cross sectional area model. This model accounts for the effects of the nanoneedle, as well as the non-circular cross sectional area for the microcantilevered beam. This last parameter was taken into consideration by updating the value for the torsional rigidity of our model

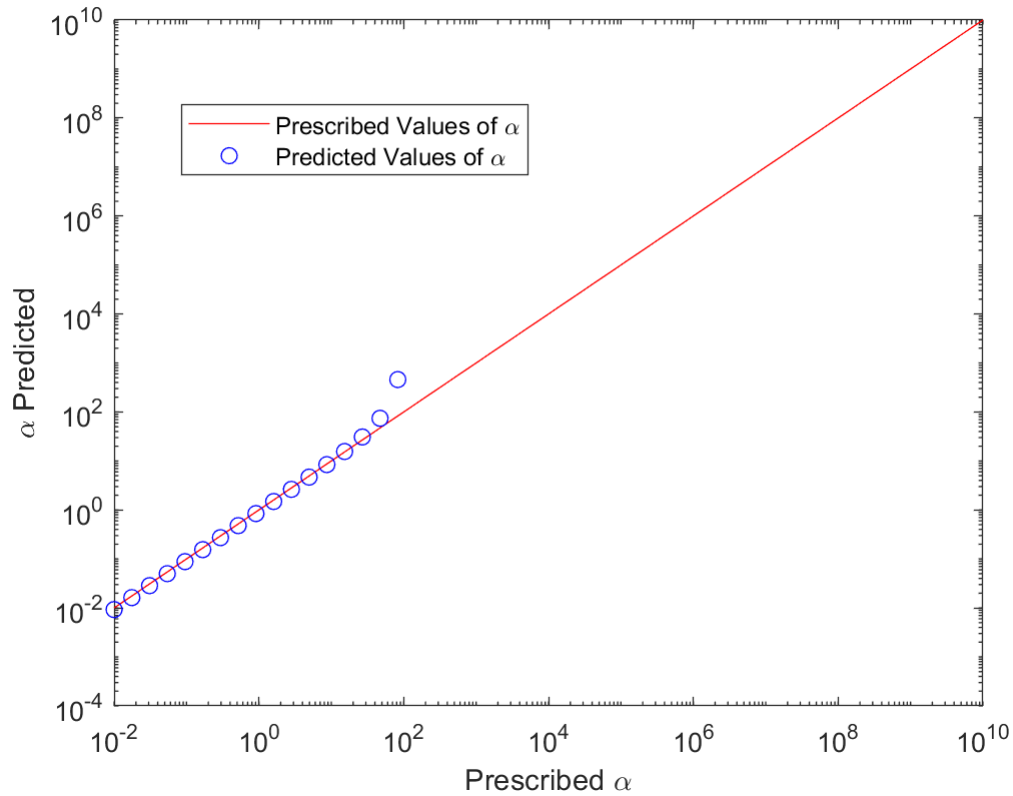


Fig. 3.9. Prescribed values for α array [Red Line] versus predicted value for α array [Blue Dots] for the updated proposed model for non-circular cross sectional areas for the first mode of transverse vibration, where the blue dots not seen on the plot are ignored negative values.

from Equation 2.79. The graph in Figure 3.9 shows the performance of the updated model versus the prescribed values for α from the 3D finite element model.

Figure 3.10 shows the performance of our model for the prescribed values of α . We can observe that the error is still contained within 10 percent for the first mode of vibration. The effective range of the model for the first mode of vibration is from 10^{-2} to 10^2 . Once α begins to approach values of 10^3 we observe the model predictions begin to fail. The updated proposed model expands the effective range of predictions for the first mode of vibration and keeps the error margin within 10 percent as the baseline and proposed model do, as well. From previous sections, we

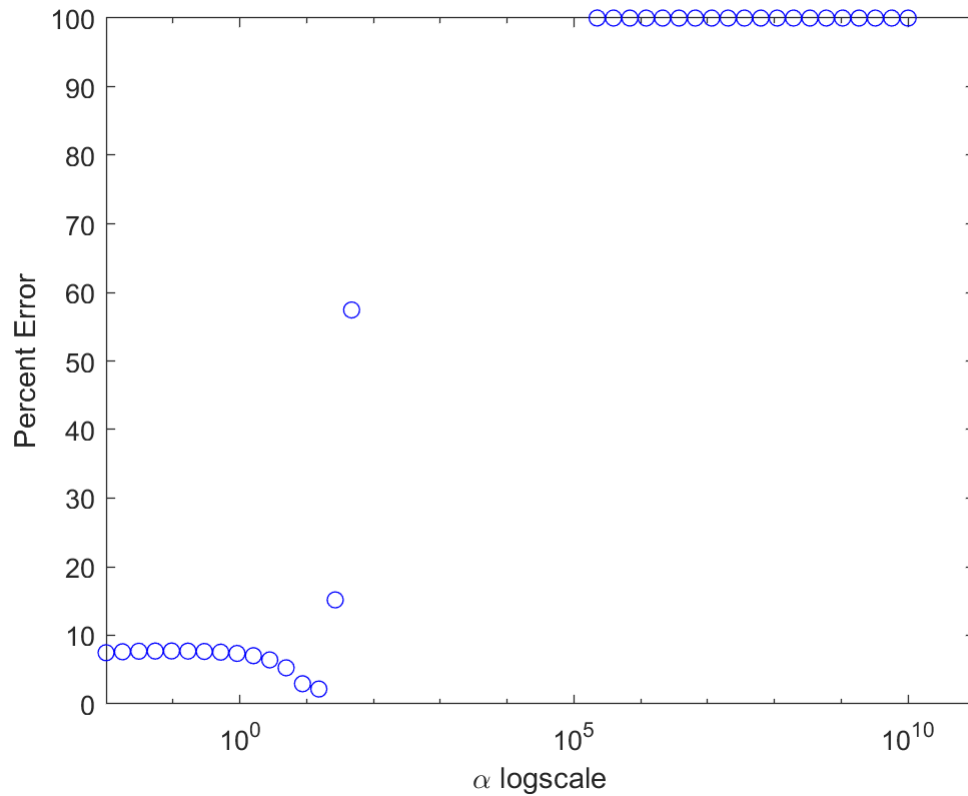


Fig. 3.10. Percent error for the individual predicted values of α for the proposed model for non-circular cross sectional areas using the information from the first mode of transverse vibration, where the cluster of points aligned at 100 percent error are simply a product of a very small predicted value for α compared to a very large prescribed value for α

have observed it is imperative to analyze the second mode's data in order to fully assess the performance of the updated proposed model.

3.3.2 Using the Second Mode of Transverse Vibration

The graph in Figure 3.11 shows the performance of our model versus the prescribed values of α . Here, similarly to the proposed model, we observe a significant increase for predictions using the second mode of vibration. Figure 3.12 shows an improvement

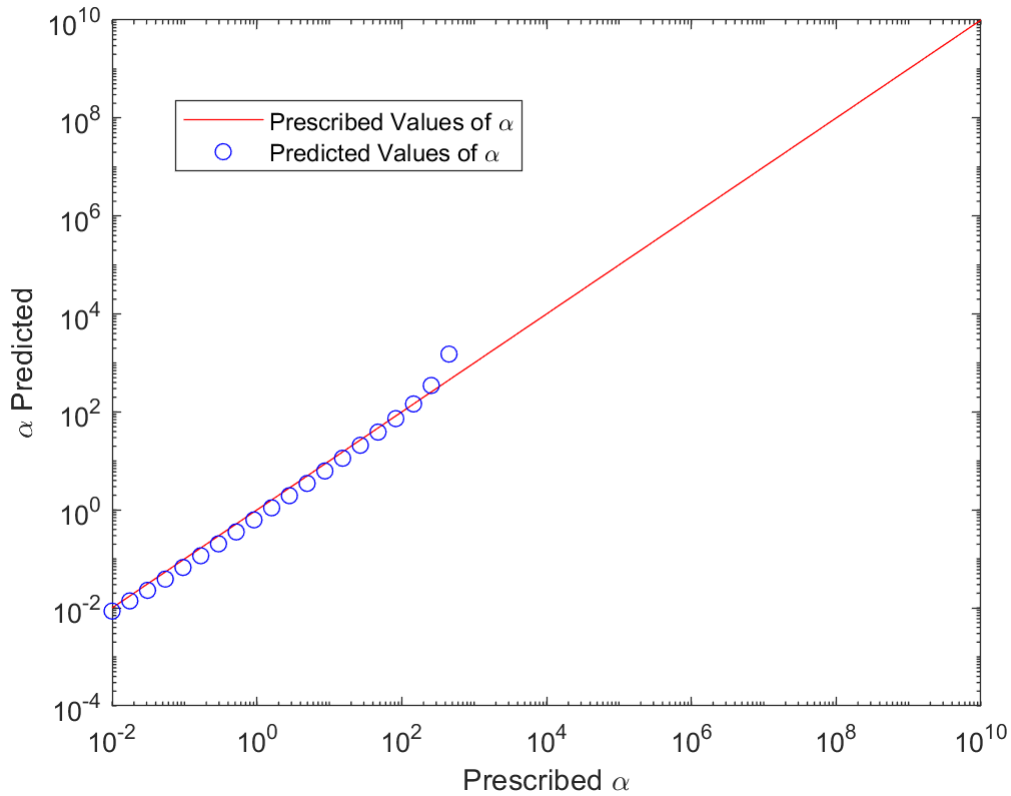


Fig. 3.11. Prescribed values for α array [Red Line] versus predicted value for α array [Blue Dots] for the updated proposed model for non-circular cross sectional areas for the second mode of transverse vibrations, where the blue dots not seen on the plot are ignored negative values.

in predictions for the updated proposed model. We have minimized the error and expanded the effective range of predictions, leading to almost 100 percent accuracy for α values of 10^2 . Our first prediction for the value of α is now almost down to a 10 percent error and we stay within 30 percent of the prescribed value for α , where the updated model seemed to exceed the 30 percent window by a few percent. It appears that our proposed model is the most accurate for predictions of α for values of 10^2 for the second mode of vibrations and performs well under 10 percent error for the first mode of vibration. In the following section, we observe how this data compares

by narrowing the plot domain in order to only inspect the data for α from 10^{-2} to 10^3 . This is the total effective range for all three models combined.

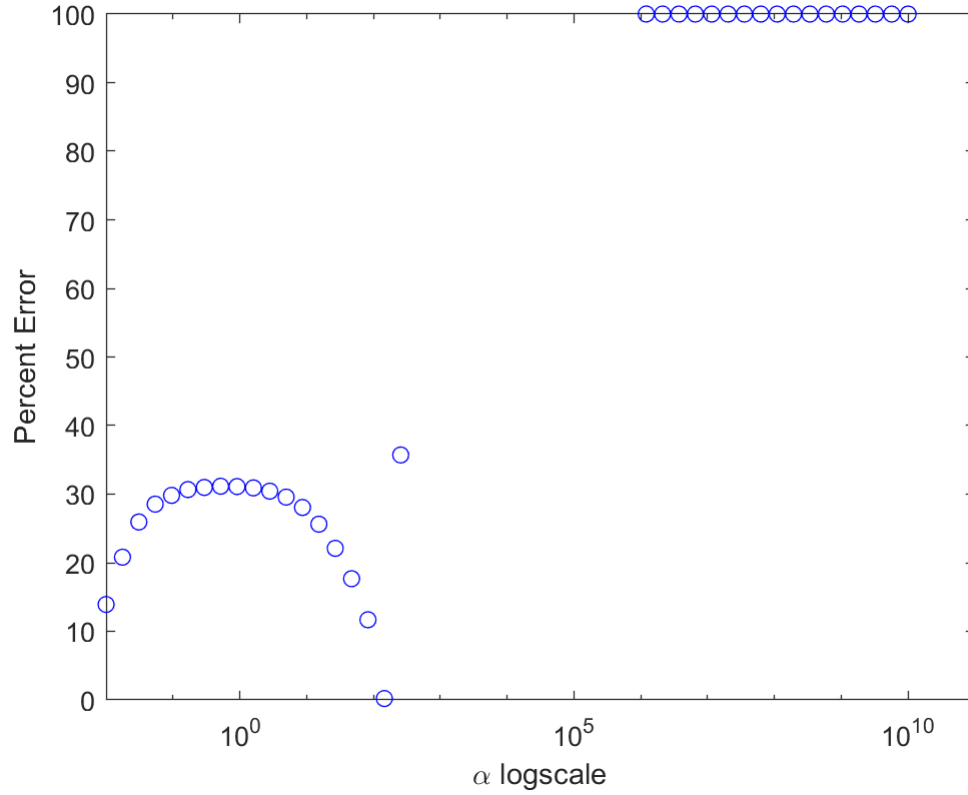


Fig. 3.12. Percent error for the individual predicted values of α for the proposed model for non-circular cross sectional areas from the second mode of vibration, where the cluster of points aligned at 100 percent error are simply a product of a very small predicted value for α compared to a very large prescribed value for α .

3.4 Discussion: Percent Error for Effective Range of α

3.4.1 First Mode Discussion

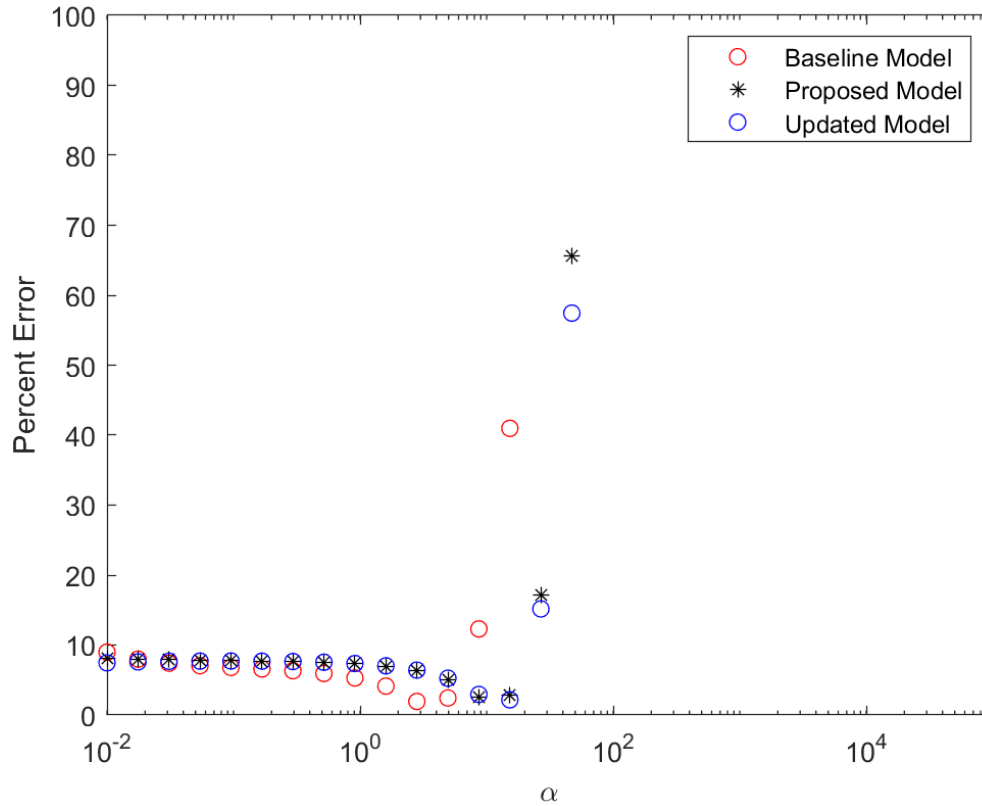


Fig. 3.13. Percent error for baseline model, proposed model and updated model for predictions of α using data from the first mode of vibration.

From Figure 3.13, for the first value of α at 10^{-2} , all three models have predictions within the 10 percent accuracy range. The blue dots represent the percent difference between the updated proposed model predictions for α and the prescribed values of α . The red dots represent the percent difference between the baseline model predictions and the prescribed values of α . The black asterisks represent the percent difference for the proposed model and the prescribed values of α . We can observe that the

percent error for the first predicted value of α is the lowest for the updated proposed model and the highest for the baseline model, with the proposed model performing better than the baseline, but worse than the updated proposed model. After the first prediction all three models essentially perform equally for the effective range of 10^{-2} to 10^0 . Once the predictions for α reach the value of 10^0 the baseline model performs slightly better than both the proposed and updated proposed models, but as we approach values of 10^1 the model fails and results in a spike of percent error. Meanwhile, both our proposed and updated models change from a constant 7 percent error to an improved 2 percent error for values of α equal to 10^1 . Therefore both our models have predictions within the 7 percent range for the the effective range for α of 10^{-2} to 10^0 and also provide an increase in accuracy for values of α equal to 10^1 . As the values of α approach values of 10^2 , both our models begin to fail. Therefore, both our proposed and updated proposed models extend the effective range for predictions of α by 1 decade, thus improving the range of predictions for CR AFM application. In the following section, we show the use of the second mode of transverse vibration to access values of α equal to 10^2 .

3.4.2 Second Mode Discussion

The improvement in predictions for values of α using the data from the second mode of vibration can be seen in Figure 3.14. The improvement from the baseline model is evident when observing the results for the second mode, where the baseline model fails to predict any values within the 10 percent range. The baseline predictions start almost at a 100 percent error, then slowly improve, but not enough for reliable predictions. Meanwhile, the proposed model and the updated proposed model reduce the percent error down to 20 and 12 percent, respectively. Both models reach a

maximum of 30 percent error, but then reach about zero percent error for values of α equal to 10^2 .

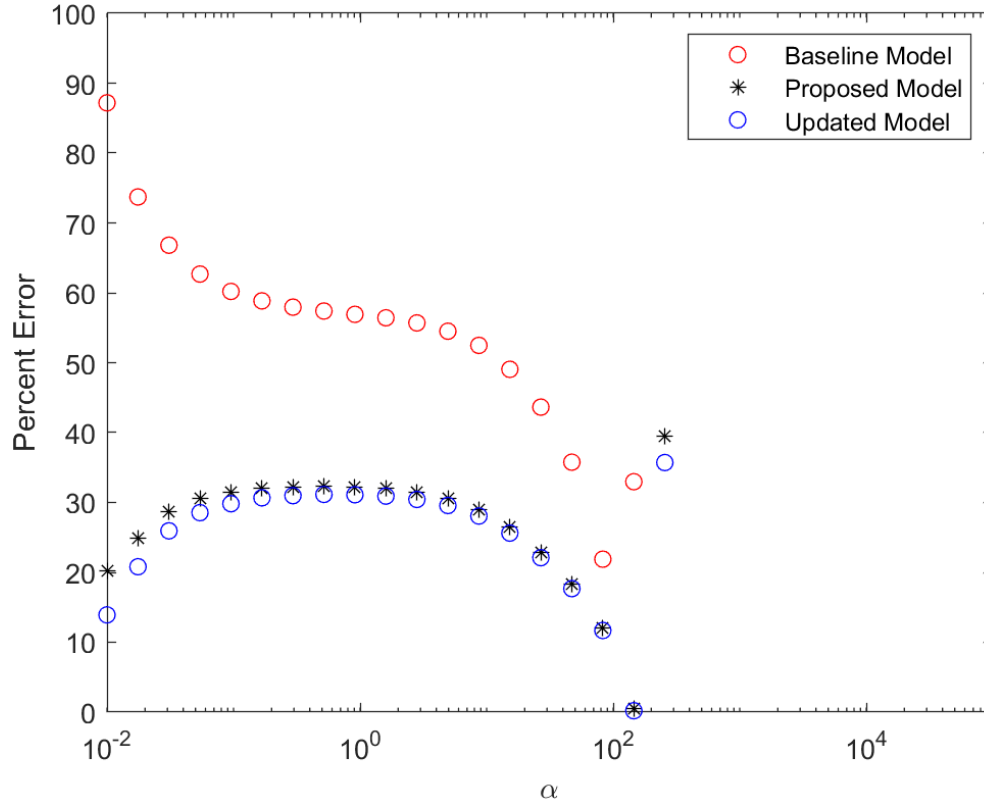


Fig. 3.14. Percent error for baseline model, proposed model and updated model for predictions of α using data from the second mode of vibration.

Therefore the proposed model and updated proposed expand the effective range of predictions for values of α , and provide exact predictions for values of α of 10^2 . As we increase the modes of vibration, we shift the effective range of predictions. Therefore, with higher modes we can predict stiffer materials. With the baseline model, the second mode was inaccessible and essentially failed to output any reliable predictions. The use of higher modes, lead to shifting the window of prediction to a higher effective range. Therefore, the theoretical model needed to be updated in

order to gain access to this mode of vibration, as we can see from the percent error between the baseline model and both the proposed and updated model.

4. FUTURE WORK

The limitations of the model need to be better understood. Therefore, in order to tune the theoretical model, different tip geometries and locations should be analyzed. The best way to calibrate the model is by testing it for multiple trials and scenarios, in order to find the best value for the non-dimensional parameters. One possible way to increase the fidelity of the model is by adding a parameter which characterizes the flexible regime of the nanoneedle. In the 3D finite element model, the nanoneedle was modeled as a rigid body, but in reality there would be some bending of the needle. The deflections of the nanoneedle would be smaller than those of the microcantilevered beam, since the nanoneedles are usually made of chromium and the microcantilevered beam from silicon or silicon nitrate. The incorporation of a pinned boundary condition and torsional springs in the theoretical model could increase the decrease the percent error by accurately more representing the nanoneedle's dynamic behavior while in contact resonance.

Since the application of the TMT is usually for softer samples, we can narrow down the effective ranges of α next. Meaning, we can set the upper limit of predictions for α at 10^2 and begin to re-calibrate based on the methods implemented. This would include now perhaps also expanding the effective range to 10^{-3} and see how the models perform in that range. It is key to understand the features of the probe and the effects that are affecting the dynamic response of the AFM probe. In order to better represent reality, we must find quantifiable ways to develop these parameters and calibrate them for material property prediction. Therefore, further investigation of the different responses that occur during higher modes of vibration needs to be

done. Rigorous work on varying geometries and locations will results in a better tailoring of these theoretical models in order to ensure accuracy.

Conclusion

The use of CR AFM as a property retrieval technique involves the incorporation of a theoretical model. The theoretical model is intended to be a mathematical approximation of a desired physical model. In this case, the physical model is the AFM probe, which consists of a microcantilevered beam with a small sensor tip located at the free end. By using mathematical techniques, such as Euler-Bernoulli beam theory, and applying adequate boundary conditions, we tailor the mathematical model in order to represent the AFM probe. For the use of non-traditional experimental setups, such as the TMT, which involves the addition of a long nanoneedle on the traditional sensing tip, a theoretical model must be derived in order to account for the long-tip dynamics which affect the AFM probe's response. We propose and derive a theoretical model tailor particularly for the TMT for the use of CR AFM in order to characterize a sample's stiffness. After deriving the proposed model we increase fidelity by incorporating an update to the mathematical model. This update accounts for the non-circular cross sectional area of the AFM probe. The performance of both the proposed and updated models is compared and assessed versus the performance of the baseline model, which does not account for the nanoneedle tip dynamics. All three models perform within the 10 percent range, for an effective range of α from 10^{-2} to 10^0 for the data from the first mode of vibration. The baseline model failed to predict any value for α past that. Meanwhile, both our models successfully extended the effective range to 10^1 and provided an increase in accuracy. For the second mode of vibration, the baseline model failed to predict any reliable values for α . On the other hand, both our models contained the percent error to a maximum of 30 percent and extended to the effective range to values for α of 10^2 , with nearly zero percent error. Both the proposed and updated models must be calibrated before using them

for α predictions. Therefore, close attention must be paid during these procedures and the implementation of the techniques, as well.

REFERENCES

- [1] L.-Y. Chen, J.-Q. Xu, H. Choi, M. Pozuelo, X. Ma, S. Bhowmick, J.-M. Yang, S. Mathaudhu, and X.-C. Li, "Processing and properties of magnesium containing a dense uniform dispersion of nanoparticles," *Nature*, vol. 528, no. 7583, p. 539, 2015.
- [2] B. Yu and F. Moussy, "Epoxy enhanced polymer membrane to increase durability of biosensors," May 19 2009, uS Patent 7,534,330.
- [3] F. Li, L. Li, X. Liao, and Y. Wang, "Precise pore size tuning and surface modifications of polymeric membranes using the atomic layer deposition technique," *Journal of membrane science*, vol. 385, pp. 1–9, 2011.
- [4] G. Binnig, H. Rohrer, C. Gerber, and E. Weibel, "Surface studies by scanning tunneling microscopy," *Physical review letters*, vol. 49, no. 1, p. 57, 1982.
- [5] D. B. Williams and C. B. Carter, "The transmission electron microscope," in *Transmission electron microscopy*. Springer, 1996, pp. 3–17.
- [6] G. Binnig, C. F. Quate, and C. Gerber, "Atomic force microscope," *Physical review letters*, vol. 56, no. 9, p. 930, 1986.
- [7] X. Hu, G. Li, and J. C. Yu, "Design, fabrication, and modification of nanostructured semiconductor materials for environmental and energy applications," *Langmuir*, vol. 26, no. 5, pp. 3031–3039, 2009.
- [8] A. Korkin, P. Krstić, and J. C. Wells, *Nanotechnology for electronics, photonics, and renewable energy*. Springer, 2010, vol. 78.
- [9] K. Jain and V. Jain, "Impact of nanotechnology on healthcare-applications in cell therapy and tissue engineering," *Nanotech. L. & Bus.*, vol. 3, p. 411, 2006.
- [10] J. O. Hirschfelder and W. J. Meath, "The nature of intermolecular forces," *Advances in chemical physics: intermolecular forces*, pp. 3–106, 1967.
- [11] B. R. A. Nijboer, "The diffraction theory of aberrations," Ph.D. dissertation, Wolters, 1942.
- [12] C. A. Schuh, "Nanoindentation studies of materials," *Materials today*, vol. 9, no. 5, pp. 32–40, 2006.
- [13] N. A. Geisse, "Afm and combined optical techniques," *Materials today*, vol. 12, no. 7-8, pp. 40–45, 2009.
- [14] L. Kurbatov, S. Shakhidzhanov, L. Bystrova, K. VV, and K. SI, "Investigation of superluminescence emitted by a gallium arsenide diode," *SOVIET PHYSICS SEMICONDUCTORS-USSR*, vol. 4, no. 11, pp. 1739–+, 1971.

- [15] D. Chicea, B. Neamtu, R. Chicea, and L. Chicea, "The application of afm for biological samples imaging." *Digest Journal of Nanomaterials & Biostructures (DJNB)*, vol. 5, no. 4, 2010.
- [16] P. Yuya, D. Hurley, and J. A. Turner, "Contact-resonance atomic force microscopy for viscoelasticity," *Journal of Applied Physics*, vol. 104, no. 7, p. 074916, 2008.
- [17] D. C. Hurley, "Contact resonance force microscopy techniques for nanomechanical measurements," in *Applied scanning probe methods XI*. Springer, 2009, pp. 97–138.
- [18] C. A. Putman, K. O. Van der Werf, B. G. De Groot, N. F. Van Hulst, and J. Greve, "Tapping mode atomic force microscopy in liquid," *Applied physics letters*, vol. 64, no. 18, pp. 2454–2456, 1994.
- [19] M. H. Korayem, H. J. Sharahi, and A. H. Korayem, "Comparison of frequency response of atomic force microscopy cantilevers under tip-sample interaction in air and liquids," *Scientia Iranica*, vol. 19, no. 1, pp. 106–112, 2012.
- [20] J. E. Sader, "Frequency response of cantilever beams immersed in viscous fluids with applications to the atomic force microscope," *Journal of applied physics*, vol. 84, no. 1, pp. 64–76, 1998.
- [21] R. C. Tung, J. P. Killgore, and D. C. Hurley, "Liquid contact resonance atomic force microscopy via experimental reconstruction of the hydrodynamic function," *Journal of Applied Physics*, vol. 115, no. 22, p. 224904, 2014.
- [22] M. Minary-Jolandan, A. Tajik, N. Wang, and M.-F. Yu, "Intrinsically high-q dynamic afm imaging in liquid with a significantly extended needle tip," *Nanotechnology*, vol. 23, no. 23, p. 235704, 2012.
- [23] G. Ramalingam and P. Reinke, "Growth of ni and ni-cr alloy thin films on mgo (001): Effect of alloy composition on surface morphology," *Journal of Applied Physics*, vol. 120, no. 22, p. 225302, 2016.
- [24] J. P. Killgore, D. Yablon, A. Tsou, A. Gannepalli, P. Yuya, J. A. Turner, R. Proksch, and D. Hurley, "Viscoelastic property mapping with contact resonance force microscopy," *Langmuir*, vol. 27, no. 23, pp. 13 983–13 987, 2011.
- [25] P. Yuya, D. Hurley, and J. A. Turner, "Relationship between q-factor and sample damping for contact resonance atomic force microscope measurement of viscoelastic properties," *Journal of Applied Physics*, vol. 109, no. 11, p. 113528, 2011.
- [26] S. S. Rao and F. F. Yap, *Mechanical vibrations*. Prentice hall Upper Saddle River, 2011, vol. 4.
- [27] S. S. Rao, *Vibration of continuous systems*. Wiley Online Library, 2007, vol. 464.